Journal Pre-proofs

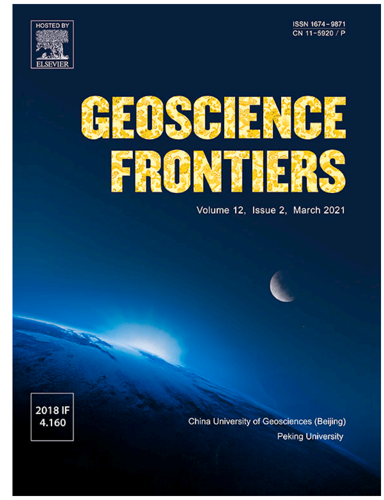

Research Paper

High-resolution astronomical records of shale strata in faulted lake basins and implications for the sedimentary process of laminated sediments

Xianzheng Zhao, Xiaoping Liu, Huan Liu, Fengming Jin, Xiugang Pu, Biao Sun, Zhannan Shi

PII: S1674-9871(24)00198-1
DOI: https://doi.org/10.1016/j.gsf.2024.101974
Reference: GSF 101974

To appear in: *Geoscience Frontiers*

Received Date: 23 February 2024
Revised Date: 1 September 2024
Accepted Date: 23 November 2024

Please cite this article as: X. Zhao, X. Liu, H. Liu, F. Jin, X. Pu, B. Sun, Z. Shi, High-resolution astronomical records of shale strata in faulted lake basins and implications for the sedimentary process of laminated sediments, *Geoscience Frontiers* (2024), doi: https://doi.org/10.1016/j.gsf.2024.101974

Research Paper

High-resolution astronomical records of shale strata in faulted lake basins and implications for the sedimentary process of laminated sediments

Xianzheng Zhao[a,b,c], Xiaoping Liu[a,d,*], Huan Liu[a,d], Fengming Jin[c], Xiugang Pu[c], Biao Sun[a,d], Zhannan Shi[c]

[a] *National Key Laboratory of Petroleum Resources and Engineering, China University of Petroleum (Beijing), Beijing 102249, China*

[b] *China Petroleum Consulting Center, Beijing 100724, China*

[c] *Dagang Oil Field Company of PetroChina, Tianjin 300280, China*

[d] College of Geosciences, China University of Petroleum (Beijing), Beijing 102249, China

*Corresponding author. E-mail address: liuxiaoping@cup.edu.cn

Abstract

Lamina structure, a typical feature of shale, has significant implications for hydrocarbon generation, shale oil and gas reservoir evaluation, and palaeoenvironmental studies. In this study, we conducted a high-resolution astronomical analysis of shale strata from the Kongdian Formation in the Cangdong Sag, Bohai Bay Basin, China, and performed macroscopic and microscopic textural characterization of core samples. The time series analysis of the G108-8 Well indicates that stratigraphic cycles of 113.2–25.3 m, 12.7–7.8 m, 4.7–2.7 m, and 2.3–1.3 m are controlled by long eccentricity, short eccentricity, obliquity, and precession, respectively. The sedimentary accumulation rate (SAR) is estimated to be approximately 20.3 cm/kyr. The core description reveals that Ek_2 primarily consists of laminated shale with individual laminae less than 1 cm in thickness. Using a polarizing microscope, the average thickness of a single lamina is approximately 250 μm, with most laminae being less than 400 μm. We constructed a time-depth model for lacustrine laminated sediments and compared it with other ancient lacustrine strata and modern lakes. The sediment accumulation rate of ancient lacustrine strata ranges from 1.3 to 20.3 cm/kyr. The sedimentation rate of shale and the thickness distribution of individual laminae provide evidence for the annual nature of the lamina couplets. Finally, we propose a simplified model to illustrate the sedimentation process, emphasizing the record of laminated sediments in semi-deep to deep facies. Our results contribute to the

understanding of lacustrine sedimentary processes, laminated sedimentary records, organic matter enrichment processes, palaeoenvironments, and their potential relationships.

Keywords: Cangdong Sag; Lacustrine laminated sediments; Astrochronological record; Sedimentation rate; Varves

Handling Editor: Yirang Jang

1. Introduction

Laminated sediments are widely present in nature, including tree rings, speleothems, corals, and varves. The study of laminated structures in fine-grained sediments dates back to 1862, with numerous results on laminated rocks published in the 1950s (Mckee and Gorden, 1953; Ingram, 1954). The study of laminae and its application in palaeoclimate research has also accelerated the development of related theories and techniques (Ingemar, 1976; Simola, 1977). In the last 30 years, with the increasing attention paid to climate change, environmental research, and the advent of the shale oil and gas revolution, the study of laminated sediments has experienced an unprecedented boom (Davis, 2018; Zou et al., 2020; Hou et al., 2021, 2022). At present, there is no unified understanding of the genetic mechanisms behind the laminated structures in fine-grained sedimentary rocks. The traditional sedimentological concept holds that fine-grained sediments and laminae are usually deposited and preserved in low-energy environments through suspension and flocculation (Tylmann et al., 2012; Wu et al., 2022; Xu et al., 2023). Physical simulations of shale sedimentation have shown that shale can be deposited under certain hydrodynamic conditions through bottom-flow transport (Schieber et al., 2007; Li and Schieber, 2015; Yawar and Schieber, 2017; Lu et al., 2021). Previous studies on sampling in modern lake sediment systems have found that horizontal laminae are mainly developed in deep-water areas with weak energy, while nearshore shallow-water zones are homogenous, with few laminated structures (Tylmann et al., 2012; Zolitschka et al., 2015). Through high-precision dating of modern sediments, the one-year genesis mechanism of horizontal laminae in deep-water areas has been preliminarily confirmed, and the "varve" hypothesis has become one of the important mechanisms of laminated sediment genesis (Zhou et al., 2007; Zolitschka et al., 2015; Fagel et al., 2021; Ballo et al., 2023; Walsh et al., 2023). However, due to the limited accuracy of dating ancient sediments, it is difficult to obtain direct evidence of the one-year genesis mechanism (Allard et al., 2021; Li et al., 2022).

In recent years, the rapidly developing field of astronomical orbital cycles (Milankovitch cycles) has been widely used for the analysis of lacustrine cyclostratigraphy, such as the Cretaceous stratigraphy in the Songliao Basin (Wu et al., 2014), the Paleoproterozoic stratigraphy in the Bohai Bay Basin (Zhao et al., 2019; Ma et al., 2023), the Triassic stratigraphy in the Ordos Basin (Li et al., 2023; Wei et al., 2023), and the Permian stratigraphy in the Junggar Basin (Huang et al., 2021).

Lithological, petrographic, geophysical, and chemical parameters (e.g., color, chemical element data, magnetostratigraphic data, and natural gamma-ray logging data) that reflect palaeoclimate fluctuations have been adopted in cyclostratigraphy analysis (Shi et al., 2019; Yao et al., 2022). Through spectral analysis, wavelet transforms, filtering, and tuning methods, Milankovitch cycles within stratigraphy can be identified, providing an essential basis for establishing high-precision astronomical timescales, delineating high-frequency sequences, and studying palaeoclimate changes (Torrence and Compo, 1998; Kodama and Hinnov, 2015; Ruhl et al., 2016). Additionally, time series analysis enables the establishment of time-depth (or thickness) models in the absence of an absolute time anchor, allowing for the objective estimation of sedimentation rates (Meyers, 2015, 2019; Li et al., 2018, 2019a). Previous studies in the Dongying Sag have established a depth-age model for lacustrine fine-grained sedimentary rocks using cyclostratigraphy and described the multi-scale laminated characteristics (Shi et al., 2018, 2021). These new research methods have greatly enriched the study of climate change in the pre-Quaternary period and have provided valuable insights into the genesis mechanism of laminated sediments.

Shale oil and gas, as unconventional oil and gas resources that integrate source rock and reservoir, are also influenced by the laminae of shale reservoirs, including oil and gas content, reservoir properties, mobility, and engineering feasibility (Ma et al., 2017; Xiong et al., 2019; Jin et al., 2021; Wu et al., 2022; Xin et al., 2022; Xi et al., 2023). The exploration and development of continental shale oil in China over the past decade have confirmed that a large number of laminae are developed in the Qingshankou Formation in the Songliao Basin, the Shahejie and Kongdian Formations in the Bohai Bay Basin, the Funing Formation in the Subei Basin, the Yanchang Formation in the Ordos Basin, and the Lucaogou and Fengcheng Formations in the Junggar Basin. Among these, continuous drilling of the G108-8 Well in the Cangdong Sag reveals that the thickness of a single lamina in the second member of the Kongdian Formation (Ek_2) is mostly less than 2 mm (Pu et al., 2016; Zhao et al., 2019a, 2020; Jin et al., 2023). Felsic laminae, carbonate laminae, mixed laminae, and organic-rich laminae are frequently stacked, with a lamina density of up to 11,000 layers /m (Li and Schieber, 2015; Zhao et al., 2019b; Xi et al., 2020; Ma et al., 2022; Xu et al., 2023). The geological characteristics of Ek_2, including a high density of laminae, high organic matter content, high brittle mineral content, and low clay mineral content, provide favorable geological conditions for the exploration and development of laminated shale oil in the Huanghua Depression and also offer valuable material for the study of laminated sediments (Pu et al., 2019; Zhao et al., 2019b, 2023; Zhou et al., 2020; Liu et al., 2022; Xin et al., 2022).

In this study, we conducted core descriptions and thin section observations on four intervals from Ek_2 in the Cangdong Sag, Bohai Bay Basin (BBB). Furthermore, spectral and wavelet analyses were performed on natural gamma-ray logging data from Well G108-8, revealing the presence of the Milankovitch cycles and serving as the basis for establishing the time-thickness model. Statistical methods, such as the correlation coefficient (COCO), evolutionary correlation coefficient (eCOCO), and TimeOpt analysis, were used to determine the optimal sedimentary accumulation rate (SAR). Finally, we compared the sedimentation rates of different lacustrine shale strata and modern lake basins, and proposed a simplified model to illustrate the sedimentation process, emphasizing the record of laminated sediments in semi-deep to deep lakes.

2. Geological setting

2.1 Tectonics and sedimentary system

The BBB is a Mesozoic–Cenozoic rift basin in the basement of the North China Craton, spanning between 30° and 45°N latitude. It has a rhombus-shaped configuration and covers an area of approximately 200,000 km^2 (Fig. 1A). Its tectonic evolution has undergone both the Paleoproterozoic syn-rift and post-rift periods (Fig. 2) (Qi and Yang, 2010). Within the BBB, the Cangdong Sag is situated at the center and forms part of the Huanghua Depression. It is bordered by the Cangxian Uplift to the west and the Xuhei Uplift to the east (Fig. 1B). The second member of the Kongdian Formation was deposited during the early rifting period in the Cangdong Sag, representing an inland closed lake environment. Clastic materials in the region originate from four major provenances, and deltaic sedimentation is well-developed around the lake. The sedimentary facies exhibit regular variation from the center to the margin and can be categorized into three zones: the inner, middle, and outer rings (Pu et al., 2016; Zhao et al., 2019a, 2020, 2022) (Fig. 1C).

The age of the Kongdian Formation is still somewhat controversial due to the absence of absolute age constraints. However, chronostratigraphic studies in the Bohai Bay Basin have made significant progress. Yao et al. (1994) employed K-Ar radioisotope dating of volcanic rocks in the Liaohe Basin, which indicated an age of approximately 65 Ma for the base of the Kongdian Formation. Although the initial age of the Shahejie deposits, as constrained by different methods, varies, the comprehensively calibrated age is 50.4 Ma (Yao et al., 1994; Liu et al., 2018b; Shi et al., 2018, 2019). This suggests that the age of the Kongdian Formation can be roughly constrained to 50.4–65 Ma (Fig. 2).

2.2 The G108-8, GD12, GD14 and G19-25 borehole

The four boreholes, G108-8, GD14, GD12, and GD19-25, are all situated in semi-deep to deep lake facies, as illustrated in Fig. 1C. G108-8 was drilled through the entire Ek_2, with an actual core length of 495.7 m and a recovery rate of 99.1%. The GD14, GD12, and GD19-25 wells contain partial continuous cores with drill core lengths of 68.5 m, 71.6 m, and 45.1 m, respectively. A detailed core description, including centimeter-scale lithology, X-ray diffraction (XRD), and related depositional features, was conducted on the four wells (Yan et al., 2015, 2017). The Ek_2 is divided into four sub-members (Pu et al., 2015). The lower part of Sub-member 4 (Ek_2^4) mainly consists of sandstone and light grey mudstone, while the upper part of Ek_2^4 to Sub-member 1 (Ek_2^1) primarily consists of dark felsic shale, mixed shale, and light gray dolomite.

Notably, in the G108-8 well, a deep-water gravity flow siltstone is prominently developed at the top of Sub-member 2 (Ek_2^2). This siltstone exhibits distinct logging curve characteristics, such as high gamma and low resistivity, which make it suitable as a correlation marker bed across the four wells (see Fig. 3).

3. Methodology

3.1 Core description and thin section observation

The macroscopic and microscopic characteristics of the laminae were thoroughly examined through core descriptions and thin-section observations. These analyses specifically focused on the shale sections of four intervals, as depicted in Figs. 1 and 4. Initially, the core samples were cut and polished to facilitate a detailed core description. This process involved continuous scanning and polishing of the core surface under both natural and fluorescent light, effectively enhancing the visibility of laminae boundaries. For thin-section observations, the prepared thin sections were examined at the China University of Petroleum (East China), following the SY/T5368-2000 standard protocol. These thin sections were carefully observed using a Zeiss Axioskop 40 polarizing microscope, and microphotographs were captured to document the findings.

3.2 Natural gamma-ray (GR) logging data and time series analysis

Gamma-ray (GR) logging is routinely used for lithological characterization. The concentrations of naturally occurring radioactive materials measured by GR can reflect changes in lithology, which are influenced by the depositional environment and terrestrial inputs (Li et al., 2019b). Variations in astronomical cycles lead to cyclic changes in the amount of solar insolation on the Earth's surface, regulating environmental conditions such as climate. Previous work has shown that GR is one of the most sensitive paleoclimate indicators for preserving astronomically forced climate signals and has been widely used in paleoclimate and paleoenvironmental investigations (Meyers, 2015; Ruhl et al., 2016). The G108-8 well in the Cangdong Sag was selected for this study because it provides the most representative and complete section of the Ek_2, with lithological data detailing the macroscopic and microscopic characteristics of the Ek_2 shale (Pu et al., 2019; Zhao et al., 2019a, 2019b). The GR series has a high sampling resolution (0.125 m) and completely covers the shale interval (2920–3350 m), encompassing the entire 430 m (Fig. 4).

Wavelet analysis of the GR data was performed to determine the distribution of strong cyclic signals throughout the GR series (Torrence and Compo, 1998). A 150.5 m (35% of the total length) 'loess' long-term trend was then removed, and power spectrum analysis was conducted using the 2π multi-taper method (MTM) (Thomson, 1982). The correlation coefficient (COCO), evolutionary correlation coefficient (eCOCO), and TimeOpt analysis were used to estimate the optimal sedimentation rate (Meyers, 2015; Li et al., 2018). COCO, eCOCO, and TimeOpt analyses evaluated sedimentation rates ranging from 1.6 to 50 cm/kyr with a step increment of 0.3 cm/kyr through 10,000 Monte Carlo simulations. Uncertainties in astronomical solutions beyond 50 Ma are high due to the chaos of the solar system, but the basic age model is based on the consistent recognition of the number of stable 405-kyr cycles in the geological data (Hilgen, 2010; Waltham, 2015). We primarily used estimates from Laskar et al. (2004) to derive solutions for periodicities at approximately 56 Ma. The above numerical analyses were performed using the Acycle 2.6 software (Li et al., 2019a).

4. Results

4.1 Characteristics of laminated sediments

Laminae are the most basic units of sedimentary bedding and are a typical characteristic of shales. The thickness of laminae is usually less than 1 cm (Ingram, 1954; Wu et al., 2022; Jiang et al., 2023), although some scholars define them as being less than 1 mm (Liu et al., 2018a; Zhang and Li, 2018). However, no consensus has been reached on this definition. The characteristics of laminae at different scales can be described by observing cores and identifying thin sections. Core observations under sunlight and fluorescence can identify laminae at the centimeter to millimeter scale, while thin sections can identify laminae at the millimeter to micrometer scale. In our study, we classified the lamina structure into three types based on the thickness of individual laminae: laminated rocks (millimeter-scale; single layer thickness less than 1 cm), layered rocks (centimeter-scale; single layer thickness between 1–10 cm), and massive rocks (decimeter-scale; single layer thickness greater than 10 cm).

Based on the scale of single lamina thickness, the structure observed in cores can be divided into massive (Fig. 5E and F), layered (Fig. 5G and H), and laminated rocks (Fig. 5C, D, I, and J). Lamina boundaries are sometimes unclear under sunlight, but using fluorescence can make the lamina interfaces clearer. Different fluorescence intensities can also reflect variations in oil content among different laminae. The total length of the four intervals is 615.2 m, of which the cumulative thickness of laminated rocks is 334.6 m, accounting for 54.4%, layered rocks total 141.5 m, accounting for 23.0%, and massive rocks total 139.1 m, accounting for 22.6% (Fig. 5A and B). The thin-section identification results show that the differences between adjacent laminae are more pronounced, with adjacent bright and dark layers forming a complete rhythmic combination, which some refer to as a "binary structure" (Fig. 6). However, because the minerals in fine-grained sedimentary rocks are mainly clay-sized particles with a cryptocrystalline structure, it is difficult for optical microscopes to accurately identify mineral types. Occasional microscopic flame configurations can be observed under the optical microscope (Fig. 6B), along with scattered coarse and silt-sized particles (Fig. 6E, F, G, and H). Previous studies using high-resolution techniques such as scanning electron microscopy have observed and analyzed the microscopic mineral composition of lacustrine shale in China, indicating that the bright laminae are mainly composed of felsic or carbonate minerals, while the dark laminae are primarily composed of clay minerals and organic matter (Fig. 6I). Statistical analysis based on observations of 357 laminated and layered samples shows that the thickness of individual laminae is less than 400 μm, with an average thickness of 250 μm (Fig. 7).

4.2 Cyclostratigraphic analysis and sediment accumulation rate (SAR)

There is generally a strong correlation between GR values and lithology, with higher GR values typically observed in shale formations and lower values in sandstone formations. Sudden changes in GR values often occur at lithological boundaries and unconformity surfaces (Fig. 4). Through wavelet transformation of the unfiltered GR data, cyclic patterns with wavelengths of 87.2 m, 38.4 m, 12.7 m, 2.3 m, and 1.7 m were identified (Fig. 8A). Spectrum analysis of the detrended GR series reveals a hierarchy of cycles with a confidence level of 95% (Fig. 8C). The ratio of wavelengths of 113.6–25.3 m, 12.7–7.8 m, 4.7–2.7 m, and 2.3–1.3 m is approximately 21:6.9:2.6:1.3, which aligns with the ratio of astronomical periods at 56 Ma (21:6.5:2.7:1.2). This may indicate that these cycles represent long eccentricity, short eccentricity, obliquity, and precession periods, respectively.

The results of COCO and eCOCO analyses of the GR series suggest that sedimentation rates of 22.4 cm/kyr, 26.9 cm/kyr, and 31.6 cm/kyr yield a null hypothesis (H_0, no astronomical drive) significance level of less than 0.01 (Fig. 9). The TimeOpt results indicate that the optimal sedimentation rate is 20.3 cm/kyr (Fig. 10). The consistency between COCO, eCOCO, and TimeOpt results supports that the SAR of the target interval is approximately 20.3 cm/kyr. Therefore, the wavelength of approximately 87.2 m is most likely to represent the 405 kyr long eccentricity signal (Fig. 8B). These results provide convincing evidence for the presence of the Milankovitch cycle in the sedimentary records of the Ek_2.

5. Discussion

5.1 Comparison of SAR in lacustrine sediments

Many factors affect the sedimentation rate of basins, and previous researchers have restored sedimentation rates from multiple perspectives. The sedimentation rate of marine shale in China is generally lower than 3 cm/kyr (Zhang et al., 2023a), while lacustrine shale varies from 1.3 cm/kyr to 19.2 cm/kyr (Fig. 11A).

The cyclostratigraphy of the Kongdian Formation in the SK-1 well of the Dongying Depression, as reported by Liu et al. (2018b), revealed an average sedimentation rate of 19.2 cm/kyr, which is similar to the 20.3 cm/kyr observed in the G108-8 well, confirming the robustness of the spectral analysis of the studied succession. In addition, for the same borehole, the results for the Shahejie-Dongying Formation show a slight decrease in sedimentation rate. The sedimentation rate of the Shahejie Formation is 7.0–22.2 cm/kyr (Liu et al., 2018b; Wang et al., 2020), while the average sedimentation rate of the Shahejie Formation in the FY1 well is 9.75 cm/kyr (Shi et al., 2018; Ma et al., 2023). The relatively younger strata of the Shuluhe Formation in the Jiuquan Basin exhibit a low sedimentation rate, with an average of 7.6 cm/kyr. In contrast, the older Xiagou Formation exhibits a higher rate of 8.5–19.8 cm/kyr, with an average of 11.4 cm/kyr (Chen et al., 2020; Yao et al., 2022). The sedimentation rates of the Permian Lucaogou Formation and Fengcheng Formation in the Junggar Basin are 8.0–10.0 cm/kyr and 9.0–19.0 cm/kyr, respectively (Huang et al., 2021, 2023; Tang et al., 2022). The sedimentation rate of the MY1 well is 9.9 cm/kyr, which somewhat differs from the SAR of approximately 16 cm/kyr calculated by Huang et al. (2021) for the FN7 well. Several research cases have been conducted in the Chang 7 Member of the Ordos Basin in central China, yet the results of the restored sedimentation rates vary considerably. The cyclostratigraphy of the Chang 7 Member, as reported by Chen et al. (2019), Zhang et al. (2019, 2023b), and Li et al. (2023), revealed apparent average sediment accumulation rates of 1.4–2.1 cm/kyr. In contrast, the cyclostratigraphy and zircon dating from the Tongchuan area of the southern Ordos Basin yield an apparent average sediment accumulation rate of 4–9.7 cm/kyr (Zhu et al., 2019; Jin et al., 2021; Chu et al., 2020, 2023; Cui et al., 2023).

In a recent study, Zhang et al. (2023a) examined and compared the sedimentation rates of 14 sets of lacustrine organic-rich shale in China. Their findings indicated that sedimentation rates generally exhibited an increasing trend with geological age, from older to newer formations. Additionally, shale from saline lacustrine environments has higher sedimentation rates than that from freshwater environments. The average sedimentation rates of the Kongdian Formation (including the Dongying Depression) are the highest among these compared lacustrine strata, which may be a terrestrial response to the "PETM" events (Tan et al., 2016). The different sedimentation rates may be subject to methodological errors and can also be attributed to the spatial heterogeneity commonly observed in continental sediments, as well as the influence of various factors related to the sedimentary environment (i.e., provenance supply, transport, and sedimentary processes). Therefore, the reasons for these differences are multifaceted and require more extensive statistical analysis and in-depth discussion.

Here, we also analyzed high-precision dating data of young sediments from four modern lake basins (Fig. 11B). Based on 175 m of continuous drilling and dating from Van Lake in Turkey, the age-depth model shows that the SAR is approximately 28 cm/kyr (Stockhecke et al., 2014). In the other three research cases from China, the maximum burial depths of sediments in Jiangcuo, Maar, and Sugan Lakes in the past 200 years are less than 30 cm. The average sedimentation rates calculated using $^{40}Ar/^{39}Ar$, ^{137}Cs, and ^{210}Pb are 70 cm/kyr, 115 cm/kyr, and 169 cm/kyr, respectively (Chu et al., 2009; Ji et al., 2021; Zhou et al., 2007), significantly higher than those of Van Lake. It is important to consider the mechanical compaction effect during the process of sediment burial depth when making comparisons, particularly in ancient strata that have already been consolidated into rock (Perrier and Quiblier, 1974). Research has shown that the volume (mainly thickness) of sediments tends to decrease with burial depth and that the compaction of shale is less than that of sandstone and limestone. The compaction rate (ratio of ancient sedimentary thickness to current thickness) after consolidation into rock can reach 2–3 (Wei et al., 2024). Therefore, the original sedimentation rate of EK_2 may exceed that of Van Lake in Turkey but is smaller than that of Jiangcuo, Maar, and Sugan Lake.

5.2 The genetic mechanism and sedimentary process of varves

This study provides evidence for the annual nature of laminae couplets by estimating the sedimentation rate of the shale beds and comparing it with the thickness distribution of individual laminae in the laminated sedimentary record. Varves with an average thickness of 250 μm in the Ek_2 of the Cangdong Sag show good consistency with those identified by Shi et al. (2021). In contrast, in the Cangdong Sag, in addition to carbonate-mineral-dominated laminae, there are also a significant number of mud-silt grade felsic laminae, indicating the sedimentation of terrestrial debris. Simultaneously, a large amount of precipitation usually accompanies a decrease in water salinity, leading to a reduction in self-generated carbonate minerals (Liu et al., 2023). Therefore, there should be a complementary effect between felsic and carbonate content. Consequently, the average thickness of laminae in the Cangdong Depression is slightly higher but still within the range of 70–300 μm (average 189 μm) observed in the Dongying Sag. The sedimentary record of the mid-to deep-facies shows continuous light and dark laminae corresponding to a one-year cycle of sedimentation (Zolitschka et al., 2015; Shi et al., 2021; Tian et al., 2024). The light laminae, predominantly composed of felsic or calcite, form during summer, while the dark laminae, comprising a mixture of clay and organic matter, are primarily deposited during winter and early spring (Figs. 6 and 12). The conditions and rates of sedimentation of organic matter, clay, felsic, and carbonate minerals in lake basins are typically variable. During spring and summer, fine-grained material from the land is transported by rivers and winds and tends to settle in the far shore areas of the lake basin, resulting in the formation of layers predominantly composed of terrestrial debris. During drought and salinization, the proportion of terrestrial material is typically relatively low. Carbonates in the water crystallize and precipitate under changes in salinity and the action of organisms, forming layers mainly composed of carbonate minerals and supplemented by terrestrial debris particles. In autumn and winter, the energy of the lake basin water decreases, and biological activity also diminishes. At this time, clay minerals and organic matter in the lake basin settle under flocculation, forming organic-rich clay laminae. Additionally, the shale strata of the Yanchang Formation in the Ordos Basin and the Lucaogou Formation in the Junggar Basin in China contain numerous pyroclastic laminae, which are typically associated with frequent volcanic eruptions (Xi et al., 2020; Wu et al., 2022). Once the annual rhythm of the laminae is established in these natural archives, their chronological sequence and the burial process of organic matter can be determined by consecutive lamina counting. This idealized simplified model cannot fully explain the genesis of massive rocks in the semi-deep facies and horizontally laminated rocks in shallow lacustrine environments. It requires further consideration of the complexity and variety of geological processes, such as the influence of water energy, bioturbation, and geological events on the formation and preservation of laminated sediments. Additionally, the potential for biased perceptions caused by single-hole views must be acknowledged.

6. Conclusion

The drilling cores from four wells and the GR series of G108-8 in the Cangdong Sag of BBB provide a record of rhythmically laminated sediments in Ek_2, opening a window for exploring lacustrine laminae. The main conclusions are as follows:

(1) We determined the thickness characteristics of the laminae through core description and thin-section identification. On a core scale, the laminations predominantly consist of shale with a thickness typically less than 1 cm. On a thin-section scale, the thickness of individual laminae is less than 400 μm, with an average of 250 μm.

(2) Time series analysis has revealed sedimentary cycles that correlate with Milankovitch cycles. The Ek_2 sediments display significant peaks at wavelengths of 113.2–25.3 m, 12.7–7.8 m, 4.7–2.7 m, and 2.3–1.3 m. Power spectrum analysis identifies peaks at 87.2 m, 38.4 m, 12.7 m, 2.3 m, and 1.7 m, aligning with signals observed in the wavelet transform. This ratio of significant peaks concurs with the periodicity ratio of astronomical cycles at 56 Ma.

(3) The genetic mechanism behind the rhythmic laminated sediment in Ek_2 can be attributed to a one-year cycle. Analysis of the sediment accumulation rate (SAR) in the 405-kyr-long GR series demonstrates that the thickness of the bright and dark couplets corresponds to one year's sediment deposition at the optimal sedimentation rate.

Acknowledgment

This study is financially supported by the National Natural Science Foundation of China (Grant No. 42072150). We are grateful to the PetroChina Dagang Oilfield Company for providing basic data access.

References

Allard, J. L., Hughes, P. D., Woodward, J. C., 2021. A radiometric dating revolution and the Quaternary glacial history of the Mediterranean mountains. Earth Sci. Rev. 223, 103844. DOI: 10.1016/j.earscirev.2021.103844.

Ballo, E. G., Bajard, M., Storen, E., Bakke, J., 2023. Using microcomputed tomography (μCT) to count varves in lake sediment sequences: Application to Lake Sagtjernet, Eastern Norway. Quat. Geochronol. 75, 101432. DOI: 10.1016/j.quageo.2023.101432.

Chen, G., Gang, W., Tang, H., Gao, G., Wang, N., Liu, L., Yang, S., Wang, Y., 2020. Astronomical cycles and variations in sediment accumulation rate of the terrestrial lower Cretaceous Xiagou Formation from the Jiuquan Basin, NW China.

Cretaceous Res. 109, 104156. DOI: 10.1016/j.cretres.2019.06.002.

Chen, G., Gang, W., Liu, Y., Wang, N., Guo, Y., Zhu, C., Cao, Q., 2019. High-resolution sediment accumulation rate determined by cyclostratigraphy and its impact on the organic matter abundance of the hydrocarbon source rock in the Yanchang Formation, Ordos Basin, China. Mar. Petrol. Geol. 103, 1-11. DOI: 10.1016/j.marpetgeo.2019.01.044.

Chu, G., Sun, Q., Gu, Z., Patrick, R., Liu, Q., Wang, K., Han, J., Liu, J., 2009. Dust records from varved lacustrine sediments of two neighboring lakes in northeastern China over the last 1400 years. Quatern. Int. 194(1), 108-118. DOI: 10.1016/j.quaint.2008.08.005.

Chu, R., Wu, H., Zhu, R., Fang, Q., Deng, S., Cui, J., Yang, T., Li, H., Cao, L., Zhang, S., 2020. Orbital forcing of Triassic megamonsoon activity documented in lacustrine sediments from Ordos Basin, China. Palaeogeogr. Palaeoclimatol. Palaeoecol. 541, 109542. DOI: 10.1016/j.palaeo.2019.109542.

Chu, R., Wu, H., Fang, Q., Huang, W., Liu, D., Zhu, R., Zhang, S., Yang, T., Wang, C., 2023. Nonlinear responses to orbital forcing inferred from an analysis of lacustrine-delta sequences spanning the Middle Triassic (Ladinian) hyperthermal episode in the Ordos Basin, China. Palaeogeogr. Palaeoclimatol. Palaeoecol. 628, 111763. DOI: 10.1016/j.palaeo.2023.111763.

Cui, J., Zhu, R., Zhang, Z., Jahandar, R., Li, Y., 2023. High resolution ID-TIMS redefines the distribution and age of the main Mesozoic lacustrine hydrocarbon Source Rocks in the Ordos Basin, China. Acta Geologica Sinica 97, 581–588. DOI: 10.1111/1755-6724.14990.

Davis, L. A., 2018. The shale oil and gas revolution. Engineering 4(4), 438-439. DOI: 10.1016/j.eng.2018.06.003.

Fagel, N., Pedreros, P., Alvarez, D., Tylmann, W., Namur, O., Da Silva , A. C. Jana , P., Araneda, A., Billy, I., Schmidt, S., Urrutia, R., 2021. Last millennium climate variability of the varved Lake Jeinimeni geochemical record from NE Chilean Patagonia. Quaternary Sci. Rev. 269, 107134. DOI: 10.1016/j.quascirev.2021.107134.

Hilgen, F.J., 2010. Astronomical dating in the 19th century. Earth Sci. Rev. 98, 65-80. DOI: 10.1016/j.earscirev.2009.10.004

Hou, L., Zou, C., Yu, Z., Luo, X., Wu, S., Zhao, Z., Lin, S., Yang, Z., Zhang, L., Wen, D., Cui, J., 2021. Quantitative assessment of the sweet spot in marine shale oil and gas based on geology, engineering, and economics: A case study from the Eagle Ford Shale, USA. Energy Strategy Rev. 38, 100713. DOI: 10.1016/j.esr.2021.100713.

Hou, L., Wu, S., Jing, Z., Jiang, X., Yu, Z., Hua, G., Su, L., Yu, C., Liao, F., Tian, H., 2022. Effects of types and content of clay minerals on reservoir effectiveness for lacustrine organic matter rich shale. Fuel 327, 125043. DOI:10.1016/j.fuel.2022.125043.

Huang, H., Gao, Y., Ma, C., Niu, L., Dong, T., Tian, X., Cheng, H., Hei, C., Tao, H., Wang, C., 2021. Astronomical constraints on the development of alkaline lake during the Carboniferous-Permian Period in North Pangea. Glob. Planet. Chang. 207, 103681. DOI: 10.1016/j.gloplacha.2021.103681.

Huang, R., Jiang, F., Chen, D., Qiu, R., Hu, T., Fang, L., Hu, M., Wu, G., Zhang, C., Lu, J., Wu, Y., Huang, L., 2023. Astrochronology and carbon-isotope stratigraphy of the Fengcheng Formation, Junggar Basin: Terrestrial evidence for the Carboniferous-Permian Boundary. Gondwana Res. 116, 1-11. DOI: 10.1016/j.gr.2022.12.016.

Ingemar, R., 1976. Annually laminated sediments in Lake Rudetjärn, Medelpad province, northern Sweden. Geologiska Föreningen i Stockholm Förhandlingar 98(4), 355-360. DOI: 10.1080/11035897609454396.

Ingram, R.L. 1954. Terminology for the thickness of stratification and parting units in sediment. GSA Bull. 86, 937-938.

Ji, K., Zhu, E., Chu, G., Hou, J., 2021. Precipitation record based on varve chronology in Jiang Co on the central Tibetan Plateau during the past 2000 years. Quaternary Sciences 41(2), 424-433. DOI: 10.11928/j.issn.1001-7410.2021.02.11.

Jiang, F., Pang, X., Yu, S., Hu, T., Bai, J., Han, G., Li, B., et al., 2015. Charging history of Paleogene deep gas in the Qibei sag, Bohai Bay Basin, China. Mar. Petrol. Geol. 67, 617-634. DOI: 10.1016/j.marpetgeo.2015.04.022.

Jiang, Z., Zhang, J., Kong, X., Xie, H., Cheng, H., Wang, L., et al., 2023. Research progress and development direction of continental shale oil and gas deposition and reservoirs in China. Acta Pet. Sin. 44, 45-71. DOI: 10.7623/syxb202301004 (in Chinese with English abstract).

Jin, F., Han, W., Shi, Z., Xu, J., Song, Y., Liu, X., Wang, D., Guan, Q., Sun, B., Ding, Y., 2023. Enrichment characteristics and production and efficiency enhancing technologies for oil in terrestrial laminar shale of Huanghua Depression in Bohai Bay Basin. Chin. Petrol. Explor. 28(3), 100-120. DOI: 10.3969/j.issn.1672-7703.2023.03.009 (in Chinese with English abstract).

Jin, X., Baranyi, V., Caggiati, M., Franceschi, M., Wall, C. J., Liu, G., Schmitz, M. D., Gianolla, P., Ogg, J. G., Lu, G., Shi, Z., Preto, N., et al., 2021. Middle Triassic lake deepening in the Ordos Basin of North China linked with global sea-level rise. Glob. Planet. Chang. 207, 103670. DOI: 10.1016/j.gloplacha.2021.103670.

Jin, Z., Zhu, R., Liang, X., Shen, Y., et al., 2021. Several issues worthy of attention in current lacustrine shale oil exploration and development. Petrol. Explor. Dev. 48, 1471-1484. DOI: 10.1016/S1876-3804(21)60303-8.

Kodama, K. and Hinnov, L. 2015. Rock Magnetic Cyclostratigraphy. John Wiley & Sons, NJ, PP. 1-163. DOI: 10.1002/9781118561294.

Laskar, J., Robutel, P., Joutel, F., Gastineau, M., Corrreia, A. C. M., Levrard, B., 2004. A long-term numerical solution for the insolation quantities of the Earth. Astron. Astrophys. 428, 261-285. DOI: 10.1051/0004-6361:20041335.

Li, M., Kump, L.R., Hinnov, L., Mann, M., et al., 2018. Tracking variable sedimentation rates and astronomical forcing in Phanerozoic paleoclimate proxy series with evolutionary correlation coefficients and hypothesis testing. Earth Planet. Sci. Lett. 501, 165-179. DOI: 10.1016/j.epsl.2018.08.041.

Li, M., Hinnov, L., Kump, L.R., 2019a. Acycle: Time-series analysis software for paleoclimate research and education. Comput. Geoscis. 127, 12-22. DOI: 10.1016/j.cageo.2019.02.011.

Li, M. Huang, C., Ogg, J., Zhang, Y., Hinnov, L., Wu, H., Chen, Z., Zou, Z., 2019b. Paleoclimate proxies for cyclostratigraphy: Comparative analysis using a Lower Triassic marine section in South China. Earth Sci. Rev. 189: 125-146. DOI: 10.1016/j.earscirev.2019.01.011.1

Li, X., Li, Y., Li, Q., Wu, L., Wang, H., Yang, C., Wei, G., Zhang, W., 2022. Progress and prospects of radiometric geochronology. Acta Geologica Sinica 96, 104-122. DOI: 10.19762/j.cnki.dizhixuebao.2022282 (in Chinese with English abstract).

Li, Y., Schieber, J., 2015. On the origin of a phosphate enriched interval in the Chattanooga Shale (Upper Devonian) of Tennessee—A combined sedimentologic, petrographic, and geochemical study. Sediment Geol. 329, 40-61. DOI: 10.1016/j.sedgeo.2015.09.005.

Li, Y., Yang, R., Loon, A.J., Dong, L., 2023. Astronomical cycles and climate change as determined from a continuous core of the Triassic Yanchang Formation (Ordos Basin, China). Mar. Petrol. Geol. 151, 106183. DOI: 10.1016/j.marpetgeo.2023.106183.

Liu, B., Shi, J., Fu, X., Lyu, Y., Sun, X., Gong, L., Bai, Y., 2018a. Petrological characteristics and shale oil enrichment of lacustrine fine-grained sedimentary system: A case study of organic-rich shale in first member of Cretaceous Qingshankou Formation in Gulong Sag, Songliao Basin, NE China. Petrol. Explor. Dev. 45, 884-894. DOI: 10.1016/S1876-3804(18)30091-0.

Liu, H., Liu, X., Liu, G., Li, G., Wang, J., Gao, Y., Sun, B., Hou, J., Liu, H., Sun, X., 2023. Sedimentary environment controls on the lacustrine shale lithofacies: A case study from the Nanpu depression, Bohai Bay Basin. Geoenergy Sci. Eng. 225, 211704. DOI: 10.1016/j.geoen.2023.211704.

Liu, Z., Huang, C., Algeo, T.J., Liu, H., Hao, Y., Du, X., Lu, Y., Cheng, B., Guo, L., Peng, L., 2018b. High-resolution astrochronological record for the Paleocene Oligocene (66–23 Ma) from the rapidly subsiding Bohai Bay Basin, northeastern China. Palaeogeogr. Palaeoclimatol. Palaeoecol. 510, 78-92. DOI: 10.1016/j.palaeo. 2017.10.030.

Liu, X., Guan, M., Jin, Z., Cao, Z., Lai, J., Zheng, L., Li, W., Sun, B., Chen, S., 2022. Pore structure evolution of lacustrine organic-rich shale from the second member of the Kongdian formation in the Cangdong Sag, Bohai Bay Basin, China. Pet. Sci. 19(2), 459-471. DOI: 10.1016/j.petsci.2021.12.010.

Lu, B., Qiu, Z., Zhou, C., Dong, D., Liang, P., 2021. Progress and prospects in the physical simulation of mudstone deposition. Acta Sedimentol. Sin. 39(4), 781-793. (in Chinese with English abstract). DOI: 10.14027/j.issn.1000-0550.2021.016.

Ma, X., Li, N., Yin, C., Li, Y., Zou, Y., Wu, S., He, F., Wang, X., Zhou, T., 2017. Hydraulic fracture propagation geometry and acoustic emission interpretation: A case study of Silurian Longmaxi Formation shale in Sichuan Basin, SW China. Petrol. Explor. Dev. 44(6), 1030-1037. DOI: 10.1016/S1876-3804(17)30116-7.

Ma, Y., Cai, X., Zhao, P., Hu, Z., Liu, H., Gao, B., Wang, Q., Li, Z., Zhang, Z., 2022. Geological characteristics and exploration practices of continental shale oil in China. Acta Geologica Sinica 96(01), 155-171. DOI: 10.19762/j.cnki.dizhixuebao.2022278 (in Chinese with English abstract).

Ma, Y., Fan, M., Li, M., Ogg, J.G., Zhang, C., Feng, J., Zhou, C., Liu, X., Lu, Y., Liu, H., Eldrett, J.S., Ma, C., 2023. East Asian lake hydrology modulated by global sea-level variations in the Eocene warmhouse. Earth Planet. Sci. Lett. 602, 117925. DOI: 10.1016/j.epsl.2022.117925.

Mckee, E.D., Weir, G.W., 1953. Terminology for stratification and cross-stratification in sedimentary rocks. GSA Bull. 64(4), 381-390. DOI: 10.1002/abio.370040210.

Meyers, S.R., 2015. The evaluation of eccentricity-related amplitude modulation and bundling in paleoclimate data: An inverse approach for astrochronologic testing and time scale optimization. Paleoceanography 30(12), 1625-1640. DOI: 10.1002/2015PA002850.

Meyers, S.R., 2019. Cyclostratigraphy and the problem of astrochronologic testing. Earth Sci. Rev. 190: 190-223. DOI: 10.1016/j.earscirev.2018.11.015.

Perrier, R., Quiblier, J., 1974. Thickness changes in sedimentary layers during compaction history; methods for quantitative evaluation. AAPG Bull. 58(3), 507–520. DOI: 10.1306/83D9142A-16C7-11D7-8645000102C1865D.

Pu, X., Han, W., Zhou, L., Chen, S., Zhang, W., Shi, Z., Yang, F., Liu, S., 2015. Lithologic Characteristics and Geological Implication of Fine-grained Sedimentation in Ek2 High Stand System Tract of Cangdong Sag, Huanghua Depression. Chin. Petrol. Explor. 20(5), 30-40. DOI: 10.11698/PED.2016.01.03 (in Chinese with English abstract).

Pu, X., Zhou, L., Han, W., Zhou, J., Wang, W., Zhang, W., Chen, S., Shi, Z., Liu, S., 2016. Geologic features of fine-grained facies sedimentation and tight oil exploration: A case from the second Member of Paleogene Kongdian Formation of Cangdong sag, Bohai Bay Basin. Petrol. Explor. Dev. 43, 26-35. DOI: 10.1016/S1876-3804(16)30003-9.

Pu, X., Jin, F., Han, W., Shi, Z., Cai, A., Wang, A., Guan, Q., Jiang, W., Zhang, W., 2019. Sweet spots geological characteristics and key exploration technologies of continental shale oil: a case study of Member 2 of Kongdian Formation in Cangdong Sag. Acta Pet. Sin. 40(08), 997-1012. DOI: 10.7623/syxb201908011 (in Chinese with English abstract).

Qi, J., Yang, Q., 2010. Cenozoic structural deformation and dynamic processes of the Bohai Bay basin province, China. Mar. Petrol. Geol. 27(4), 757-771. DOI: 10.1016/j.marpetgeo.2009.08.012.

Ruhl, M., Hesselbo, S. P., Hinnov, L., Jenkyns, H. C., Xu, W., Riding, J. B., Storm, M., Minisini, D., Ullmann, C., Leng, M., 2016. Astronomical constraints on the duration of the Early Jurassic Pliensbachian Stage and global climatic fluctuations. Earth Planet. Sci. Lett. 455, 149-165. DOI: 10.1016/j.epsl.2016.08.038.

Schieber, J., Southard, J., Thaisen, K., 2007. Accretion of mudstone beds from migrating floccule ripples. Science 318(5857), 1760-1763. DOI: 10.1126/science.1147001.

Shi, J., Jin, Z., Liu, Q., Huang, Z., Hao, Y., 2018. Terrestrial sedimentary responses to astronomically forced climate changes during the Early Paleogene in the Bohai Bay Basin, eastern China. Palaeogeogr. Palaeoclimatol. Palaeoecol. 502, 1-12. DOI: 10.1016/j.palaeo.2018.01.006.

Shi, J., Jin, Z., Liu, Q., Zhang, R., Huang, Z., 2019. Cyclostratigraphy and astronomical tuning of the middle eocene terrestrial successions in the Bohai Bay Basin, Eastern China. Glob. Planet. Chang. 174, 115-126. DOI: 10.1016/j.gloplacha.2019.01.001.

Shi, J., Jin, Z., Liu, Q., Fan, T., Gao, Z., 2021. Sunspot cycles recorded in Eocene lacustrine fine-grained sedimentary rocks in the Bohai Bay Basin, eastern China. Glob. Planet. Chang. 205, 103614. DOI: 10.1016/j.gloplacha.2021.103614.

Simola, H., 1977. Diatom succession in the formation of annually laminated sediment in Lovojärvi, a small eutrophicated lake. Annales Botanici Fennici 14, 143-148.

https://www.jstor.org/stable/43922137.

Stockhecke, M., Sturm, M., Brunner, I., Schmincke, H. U., Sumita, M., Kipfer, R., Cukur, D., Kwiecien, O., Anselmetti, F.S., 2014. Sedimentary evolution and environmental history of Lake Van (Turkey) over the past 600,000 years. Sedimentology 61(6), 1830-1861. DOI:10.1111/sed.12118.

Thomson, D.J., 1982. Spectrum estimation and harmonic analysis. Proceedings of the IEEE 70(9), 1055-1096. DOI: 10.1109/proc.1982.12433.

Tian, X., Gao, Y., Ma, J., Huang, H., Pan, J., Wang, C., 2024. Lacustrine varves in the Lower Cretaceous Yixian Formation of western Liaoning, Northeast China: Implications for seasonal to sub-decadal palaeoclimate variability associated with the Jehol Biota and "Dinosaur Pompeii". Palaeogeogr. Palaeoclimatol. Palaeoecol. 15, 646. DOI: 10.1016/j.palaeo.2024.112241.

Torrence, C., Compo, G.P., 1998. A Practical Guide to Wavelet Analysis. BAMS. 79(1), 61-78. DOI: 10.1175/1520-0477(1998)079<0061:APGTWA>2.0.CO;2.

Tylmann, W., Szpakowska, K., Ohlendorf, C., Woszczyk, M., Zolitschka, B., 2012. Conditions for deposition of annually laminated sediments in small meromictic lakes: a case study of Lake Suminko (northern Poland). J. Paleol. 47(1), 55-70. DOI: 10.1007/s10933-011-9548-3.

Wang, M., Chen, H., Huang, C., Kemp, D. B., Xu, T., Zhang, H., Li, M., 2020. Astronomical forcing and sedimentary noise modeling of lake-level changes in the Paleogene Dongpu Depression of North China. Earth Planet. Sci. Lett. 535, 116116. DOI: 10.1016/j.epsl.2020.116116.

Walsh, A. A., Blockley, S. P. E., Milner, A. M., Martin-Puertas, C., et al., 2023. Updated age constraints on key tephra markers for NW Europe based on a high-precision varve lake chronology. Quaternary Sci Rev. 300: 107897. DOI: 10.1016/j.quascirev.2022.107897.

Waltham, D., 2015. Milankovitch period uncertainties and their impact on cyclostratigraphy. J. Sediment. Res. 85(8), 990-998. DOI: 10.2110/jsr.2015.66.

Wei, R., Zhang, R., Li, M., Wang, X., Jin, Z., 2023. Obliquity forcing of lake-level changes and organic carbon burial during the Late Paleozoic Ice Age. Glob. Planet. Chang. 223, 104092. DOI: 10.1016/j.gloplacha.2023.104092.

Wei X., Xian, B., Chen, Q., 2024. Multilithologic compaction correction technique using differential method and its application in Zhuanghai Area, Shengli Oilfield. Chem. Eng. Des. Commun. 50(01), 47-49. DOI: 10.3969/j.issn.1003-6490.2024.01.016 (in Chinese with English abstract).

Wu, H., Zhang, S., Hinnov, L., Jiang, G., Yang, T., Li, H., Wang, X., Wang, C., 2014.

Cyclostratigraphy and orbital tuning of the terrestrial upper Santonian–Lower Danian in Songliao Basin, northeastern China. Earth Planet. Sci. Lett. 407, 82-95. DOI: 10.1016/j.epsl.2014.09.038.

Wu, K., Yan, B., Sun, Y., YU, L., Wang, X., 2022. Research progress on the formation mechanism and influencing factors of fine-grained sedimentary rock varves in lake basins. Acta Sedimentol. Sin. 1-29. DOI: 10.14027/j.issn.1000-0550.2022.136 (in Chinese with English abstract).

Wu, S., Zhu, R., Luo, Z., Yang, Z., Jiang, X., Lin, S., Su, L., 2022. Laminar structure of typical continental shales and reservoir quality evaluation in central-western basins in China. Chin. Petrol. Explor. 27(5), 62-72. DOI: 10.3969/j.issn.1672-7703.2022.05.006 (in Chinese with English abstract).

Xi, K., Li, K., Cao, Y., Lin, M., Niu, X., Zhu, R., Wei, X., You, Y., Liang, X., Feng, S., 2020. Laminae combination and shale oil enrichment patterns of Chang 73 sub-member organic-rich shales in the Triassic Yanchang Formation, Ordos Basin, NW China. Petrol. Explor. Dev. 47, 1342-1353. DOI: 10.1016/S1876-3804(20)60142-8.

Xi, K. Zhang, Y., Cao, Y., Gong, J., Li, K., Lin, M., 2023. Control of micro-wettability of pore-throat on shale oil occurrence: A case study of laminated shale of Permian Lucaogou Formation in Jimusar Sag, Junggar Basin, NW China. Petrol. Explor. Dev. 50, 334-345. DOI: 10.1016/S1876-3804(23)60391-X.

Xin, B., Zhao, X., Hao, F., Jin, F., Pu, X., Han, W., Xu, Q., Guo, P., Tian, J., 2022. Laminae characteristics of lacustrine shales from the Paleogene Kongdian Formation in the Cangdong Sag, Bohai Bay Basin, China: Why do laminated shales have better reservoir physical properties? Int. J. Coal Geol. 260, 104056. DOI: 10.1016/j.coal.2022.104056.

Xiong, Z., Wang, G., Cao, Y., Liang, C., Li, M., Shi, X., Zhang, B., Li, J., Fu, Y., 2019. Controlling effect of texture on fracability in lacustrine fine-grained sedimentary rocks. Mar. Petrol. Geol. 101, 195-210. DOI: 10.1016/j.marpetgeo.2018.11.020.

Xu, H., Hou, D., Löhr, S. C., Liu, Q., Jin, Z., Shi, J., Liang, X., Niu, C., George, S. C., 2023. Millimetre-scale biomarker heterogeneity in lacustrine shale identifies the nature of signal-averaging and demonstrates anaerobic respiration control on organic matter preservation and dolomitization. Geochim. Cosmochim. Acta. 348, 107-121. DOI: 10.1016/j.gca.2023.03.008.

Yan, J., Jiao, Y., Chen, S., Deng, Y., Pu, X., 2017. Soft-sediment deformation structures in deepwater fine-grained sedimentary rocks of the Member 2 of Eocene Kongdian Formation, Cangdong sag. J. Paleogeogr. 19(01), 89-98. DOI: 10.7605/gdlxb.2017.01.007 (in Chinese with English abstract).

Yan, J., Pu, X., Zhou, L., Chen, S., Han, W., 2015. Naming Method of Fine-grained Sedimentary Rocks on Basis of X-ray Diffraction Data. Chin. Petrol. Explor. 20(01), 48-54. DOI： 10.3969/j.issn.1672-7703.2015.01.005 (in Chinese with English abstract).

Yao, X., Dai, S., Li, M., Hinnov, L., 2022. Orbital eccentricity and inclination metronomes in Middle Miocene lacustrine mudstones of Jiuxi Basin, Tibet: Closing an astrochronology time gap and calibrating global cooling events. Glob. Planet. Chang. 215, 103896. DOI: 10.1016/j.gloplacha.2022.103896.

Yao, Y., Liang, H., Cai, Z., et al., 1994. Tertiary in Petroliferous Regions of China: IV, the Bohai Bay Basin. Petroleum Industry Press, Beijing, 1-76 (in Chinese).

Yawar, Z. and Schieber, J., 2017. On the origin of silt laminae in laminated shales. Sediment. Geol. 360, 22-34. DOI: 10.1016/j.sedgeo.2017.09.001.

Zhang, M., Li, Z., 2018. The lithofacies and reservoir characteristics of the fine-grained sedimentary rocks of the Permian Lucaogou Formation at the northern foot of Bogda Mountains, Junggar Basin (NW China). J. Petrol. Sci. Eng. 170, 21-39. DOI: 10.1016/j.petrol.2018.06.007.

Zhang, R., Jin, Z., Liu, Q., Li, P., Huang, Z., Shi, J., Ge, Y., Du, K., 2019. Astronomical constraints on deposition of the Middle Triassic Chang 7 lacustrine shales in the Ordos Basin, Central China. Palaeogeogr. Palaeoclimatol. Palaeoecol. 528, 87-98. DOI: 10.1016/j.palaeo.2019.04.030.

Zhang, R., Jin, Z., Zhu, R., Li, M., Hui, X., Wei, R., He, X., Zhang, Q., 2023a. Investigation of deposition rate of terrestrial organic-rich shales in China and its implications for shale oil exploration. Oil & Gas Geology 44(4), 829-845. DOI: 10. 11743/ogg20230403 (in Chinese with English abstract).

Zhang, R., Jin, Z., Li, M., Liu, Q., Li, P., Wei, R., Wang, M., He, X., 2023b. Astronomical regulation of the Middle Triassic organic-rich shales in the Ordos Basin. Quaternary Science 43(6), 1547-1561. DOI: 10.11928/j.issn.1001-7410.2023.06.04 (in Chinese with English abstract).

Zhao, K., Du, X., Lu, Y., Xiong, S., Wang, Y., 2019. Are light-dark coupled laminae in lacustrine shale seasonally controlled? A case study using astronomical tuning from 42.2 to 45.4 Ma in the Dongying Depression, Bohai Bay Basin, eastern China. Palaeogeogr. Palaeoclimatol. Palaeoecol. 528, 35-49. DOI: 10.1016/j.palaeo.2019.04.034.

Zhao, W., Zhu, R., Liu, Wei., Bian, C., Wang, K., 2023. Enrichment conditions and occurrence features of lacustrine mid-high matured shale oil in onshore China. Earth Science Frontiers 30(01), 116-127+242-259. DOI: 10.13745/j.esf.sf.2022.8.31 (in Chinese with English abstract).

Zhao, X., Zhou, L., Pu, X., Jin, F., Han, W., Shi, Z., Chen, C., Jiang, W., Guan, Q., Xu, J., Liu, X., Zhang, Wei., Ma, J., 2019a. Exploration breakthroughs and geological characteristics of continental shale oil: A case study of the Kongdian Formation in the Cangdong Sag, China. Mar. Petrol. Geol. 102, 544-556. DOI: 10.1016/j.marpetgeo.2018.12.020.

Zhao, X., Pu, X., Jin, F., Han, W., Shi, Z., Cai, A., Wang, A., Guan, Q., Jiang, W., Zhang, W., 2019b. Geological characteristics and key exploration technologies of continental shale oil sweet spots: A case study of Member 2 of Kongdian Formation in the Cangdong sag in the Huanghua depression, Bohai Bay Basin. Petroleum Res. 4(2), 97-112. DOI: 10.1016/j.ptlrs.2019.01.006.

Zhao, X., Zhou, L., Pu, X., Jin, F., Han, W., Shi, Z., Han, W., Jiang, W., Han, G., Zhang, W., Wang, H., Ma, J., 2020. Formation conditions and enrichment model of retained petroleum in lacustrine shale: A case study of the Paleogene in Huanghua depression, Bohai Bay Basin, China. Petrol. Explor. Dev. 47, 916-930. DOI: 10.1016/S1876-3804(20)60106-9.

Zhao, X., Zhou, L., Pu, X., Jin, F., Han, W., Shi, Z., Chen, C., Jiang, W., Guan, Q., Xu, J., Liu, X., Zhang, Wei., Ma, J., 2022. Theories, technologies, and practices of lacustrine shale oil exploration and development: A case study of Paleogene Kongdian Formation in Cangdong sag, Bohai Bay Basin, China. Petrol. Explor. Dev. 49, 707-718. DOI: 10.1016/S1876-3804(22)60059-4.

Zhao, X., Pu, X., Yan, J., Jin, F., Shi, Z., Chai, G., Han, W., Liu, Y., Jiang, W., Chen, C., Zhang, W., Fang, Z., Xie, D., 2023. Cycles of fine-grained sedimentation and their influences on organic matter distribution in the second member of Paleogene Kongdian Formation in Cangdong Sag, Bohai Bay Basin, East China. Petrol. Explor. Dev. 250, 534–546. DOI: 10.11698/PED.20220716.

Zhou, A., Chen, F., Qiang, M., Yang, M., Zhang, J., 2007. The discovery of annually laminated sediments (varves) from shallow Sugan Lake in inland arid China and their paleoclimatic significance. Science in China 50(8), 1218-1224. DOI: 10.1007/s11430-007-0081-1.

Zhou, L., Chen, C., Yang, F., Han, W., Guang, Q., 2020. Micropore structure characteristics and quantitative characterization methods of lacustrine shale-A case study from the member 2 of Kongdian Formation, Cangdong sag, Bohai Bay Basin. Petroleum Res. 5(2): 93-102. DOI: 10.1016/j.ptlrs.2020.01.001.

Zhu, R., Cui, J., Deng, S., Luo, Z., Lu, Y., Qi, Z., 2019. High-precision dating and geological significance of Chang 7 tuff zircon of the Triassic Yanchang Formation, Ordos Basin in central China. Acta Geologica Sinica 93, 1823-1834. DOI: 10.1111/1755-6724.14329.

Zolitschka, B., Francus, B., Ojala, A. E. K., Schimmelmann, A., 2015. Varves in lake sediments – a review. Quaternary Sci. Rev. 117: 1-41. DOI: 10.1016/j.quascirev.2015.03.019.

Zou, C., Pan, S., Jing, Z., Gao, J., Yang, Z., Wu, S., Zhao, Q., 2020. Shale oil and gas revolution and its impact. Acta Pet. Sin. 41, 1-12. DOI: 10.7623/syxb202001001 (in Chinese with English abstract).

Zou, C., Qiu, Z., Zhang, J., Li, Z., Wei, H., Liu, B., Zhao, J., Yang, T., Zhu, S., Tao, H., Zhang, F., Wang, Y., Zhang, Q., Liu, W., Liu, H., Feng, Z., Liu, D., Gao, J., Liu, R., Li, Y., 2022. Unconventional petroleum sedimentology: A key to understanding unconventional hydrocarbon accumulation. Engineering 18, 62-78. DOI: 10.1016/j.eng.2022.06.016.

Figure captions

Fig. 1. (A) The Paleogene (56 Ma) paleogeography reconstruction in Mollweide project (http://www.odsn.de). (B) An overview map of China and Bohai Bay Basin showing the location of Cangdong Sag. (C) Sedimentary system and location of four studied wells of the second member of Kongdian formation in Cangdong sag (modified after Zhao et al., 2020).

Fig. 2. The comprehensive stratigraphic column of the BBB. The ages on the left are based on the GTS2023, where those on the right are from Yao et al. (1994) and Shi et al. (2019). The Ostracoda, Characeae, and palynological biozones are from Liu et al. (2018b) and references therein. The lithology, depositional settings, and tectonic evolution of the Huanghua Depression are modified after Jiang et al. (2015).

Fig. 3. Lithological features of G108-8, GD14, GD12, and G19-25 and well correlation in Cangdong Sag (see Fig. 1C for the location of the four wells.)

Fig. 4. Stratigraphy, lithology, origin GR series, and detrended GR series of Well G108-8.

Fig. 5. Macroscope sedimentary characteristics of the four studied intervals. (A) Grain-size and sedimentary structure column of the four intervals. (B) Percentage stacking bar chart of three structure types of four intervals. (C)–(J) Macro-photographs of the typical rock.

Fig. 6. Micro-characteristics of laminated shales in Ek_2 of Cangdong Sag. (A) G108-8, 2987.93 m, the interface of the laminae is clear, consisting of 11 bright and dark cycles. (B) G108-8, 2992.79 m, the interface of the laminae is curved, with microscopic flame structure, and coarse particle deposition is developed. (C) G108-8, 3078.34 m, the laminae are continuous and the interfaces are relatively flat, consisting of 14 bright and dark cycles. (D) G108-8, 3223.89 m, the laminae are continuous and flat, consisting of 12 bright and dark cycles along the yellow line. (E) GD12, 3881.4 m, the laminae are fine and straight, with a large number of silt-sized felsic particles. (F) GD12, 3860.88 m, the laminae are flat and straight, scattered with coarse and silt-sized particles. (G) G19-25, 3370.54 m, the laminae are fine and straight, and the boundaries are clear, and scattered with coarse and silt-sized particles. (H) GD14, 4143.13 m, the laminae above the field of view are straight, while the laminae below the field of view are discontinuous, scattered with coarse and silt-sized particles. (I) G108-8, 3224.66 m, AMICS photo of laminated sample cited from Zhao et al. (2019), binary structures composed of carbonate and organic-rich clay.

Fig. 7. Bar chart and nephogram of laminae thickness distribution under a microscope. Total 3128 laminae from 357 laminated samples.

Fig. 8. (A) Lithology of the interval 1 from well G108-8. (B) Morlet wavelet transform (bottom) and plot spectrum (top) of GR series. (C) The turned GR series is shown with Gaussian filter output and the sedimentation rate calculated from the 405-kyr turned GR series, the 405-kyr cycle between E1 and E2 is relatively uncertain. (D) 2π MTM power spectrum (top) and evolutionary power spectra (bottom) of turned GR series.

Fig. 9. Results of the COCO and eCOCO analyses of the interval 1 from Well G108-8. (A) Correlation coefficient (top) and evolutionary correlation coefficient (bottom). (B) Null hypothesis (H_0, no astronomical forcing; top) and evolutionary H_0 significance level (bottom). (C) The number of contributing astronomical parameters (top) and an evolutionary number of contributing astronomical parameters (bottom).

Fig. 10. TimeOpt analysis: Pearson correlation coefficient for the precession amplitude envelope fit (r^2envelope), spectral power fit (r^2power), and combined envelope and spectral power fit (r^2opt). H_0: no astronomical forcing. The sedimentation rate tested from 1.6 to 50 cm/kyr. The Monte Carlo simulations number of TimeOpt was 10000.

Fig. 11. Differences in sedimentary accumulation rate in the lake. (A) Sedimentary

records of ancient strata. SK-1 and HE-166 data from Liu et al. (2018b), Q2-36 data from Chen et al. (2020), N36 data from Li et al. (2023), FN7 data from Huang et al. (2021), WHLX Section data from Yao et al. (2022), FY1 data from Shi et al. (2018) and Ma et al. (2023), SK-1n data from Wu et al. (2014), Y1011 data from Zhang et al. (2023b), YY1 data from Jin et al. (2021) and Chu et al. (2023). (B) Laminated sediments records of modern lakes. Van data from Stockhecke et al. (2014), Jiangco (JC) data from Ji et al. (2021), Maar (MA) data from Chu et al. (2009), and Sugan (SG) data from Zhou et al. (2007).

Fig. 12. Simplified conceptual and depositional models for lacustrine sedimentation processes and laminated sedimentary record. The depiction of geological events (i.e., volcanic and hydrothermal are not present in this study) is inspired by the Middle Triassic in the Ordos Basin (Zou et al., 2022), the Early Permian in the Junggar Basin (Huang et al., 2021) and the Early Cretaceous in the western Liaoning (Tian et al., 2024).

Highlights:

- Lacustrine shale from Ek_2 in Cangdong Sag show clear annual sedimentary records.
- Sedimentation rate of the Ek_2 is 20.3 cm/kyr based on time series analysis.
- Time-thickness model helps explaining the genesis of annually laminated sediments (Varve).

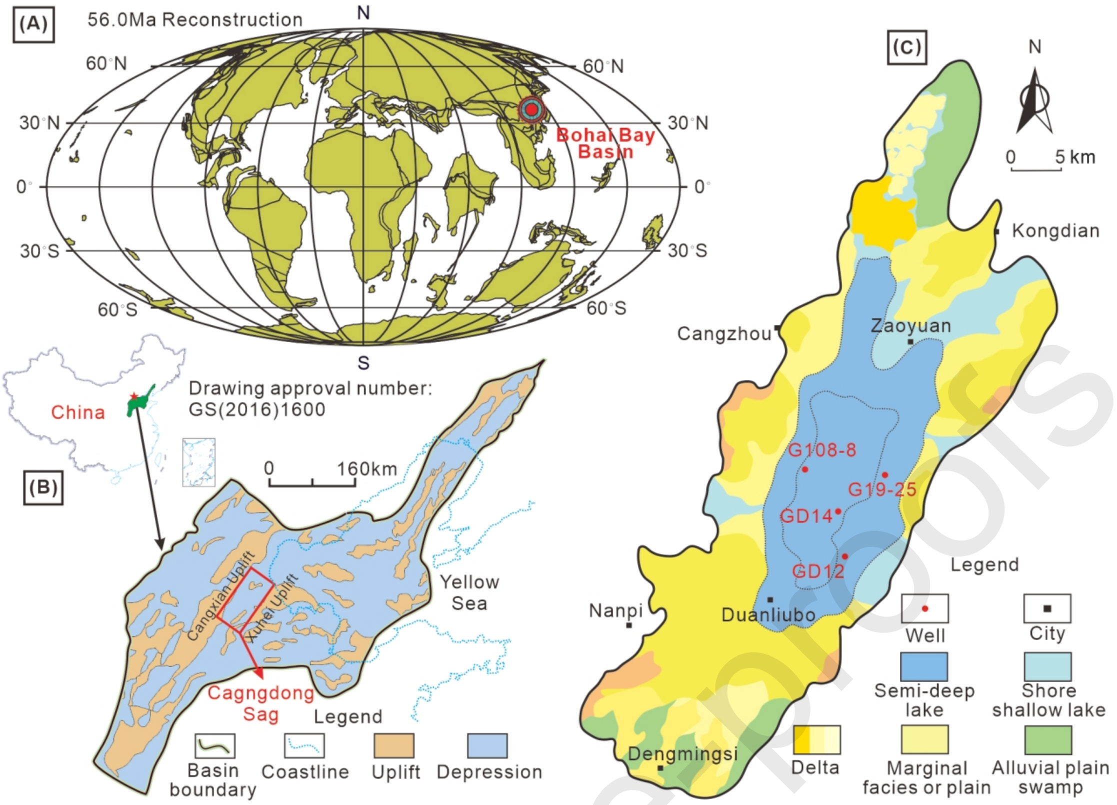
(A)
56.0Ma Reconstruction
N
S
60°N
30°N
0°
30°S
60°S
Bohai Bay Basin
China
Drawing approval number: GS(2016)1600
(B)
0 160km
Cangxian Uplift
Xuhei Uplift
Cagngdong Sag
Yellow Sea
Legend
Basin boundary
Coastline
Uplift
Depression
(C)
N
0 5 km
Kongdian
Cangzhou
Zaoyuan
G108-8
G19-25
GD14
GD12
Nanpi
Duanliubo
Dengmingsi
Legend
Well
City
Semi-deep lake
Shore shallow lake
Delta
Marginal facies or plain
Alluvial plain swamp

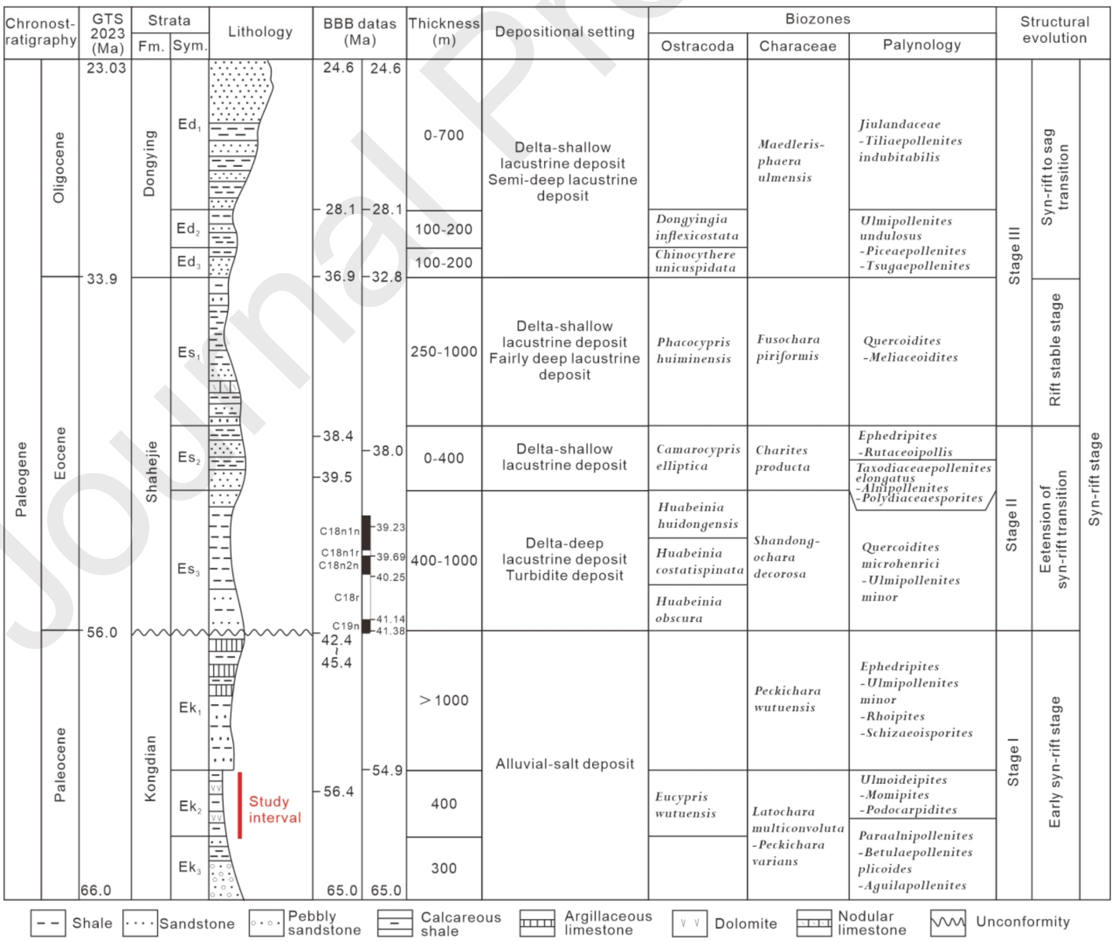
Chronostratigraphy
GTS 2023 (Ma)
Strata
Fm.
Sym.
Lithology
BBB datas (Ma)
Thickness (m)
Depositional setting
Biozones
Ostracoda
Characeae
Palynology
Structural evolution
Paleogene
Oligocene
Eocene
Paleocene
Dongying
Shahejie
Kongdian
Study interval
Delta-shallow lacustrine deposit Semi-deep lacustrine deposit
Delta-shallow lacustrine deposit Fairly deep lacustrine deposit
Delta-shallow lacustrine deposit
Delta-deep lacustrine deposit Turbidite deposit
Alluvial-salt deposit
Stage III
Stage II
Stage I
Syn-rift to sag transition
Rift stable stage
Eetension of syn-rift transition
Early syn-rift stage
Syn-rift stage
Shale
Sandstone
Pebbly sandstone
Calcareous shale
Argillaceous limestone
Dolomite
Nodular limestone
Unconformity

819 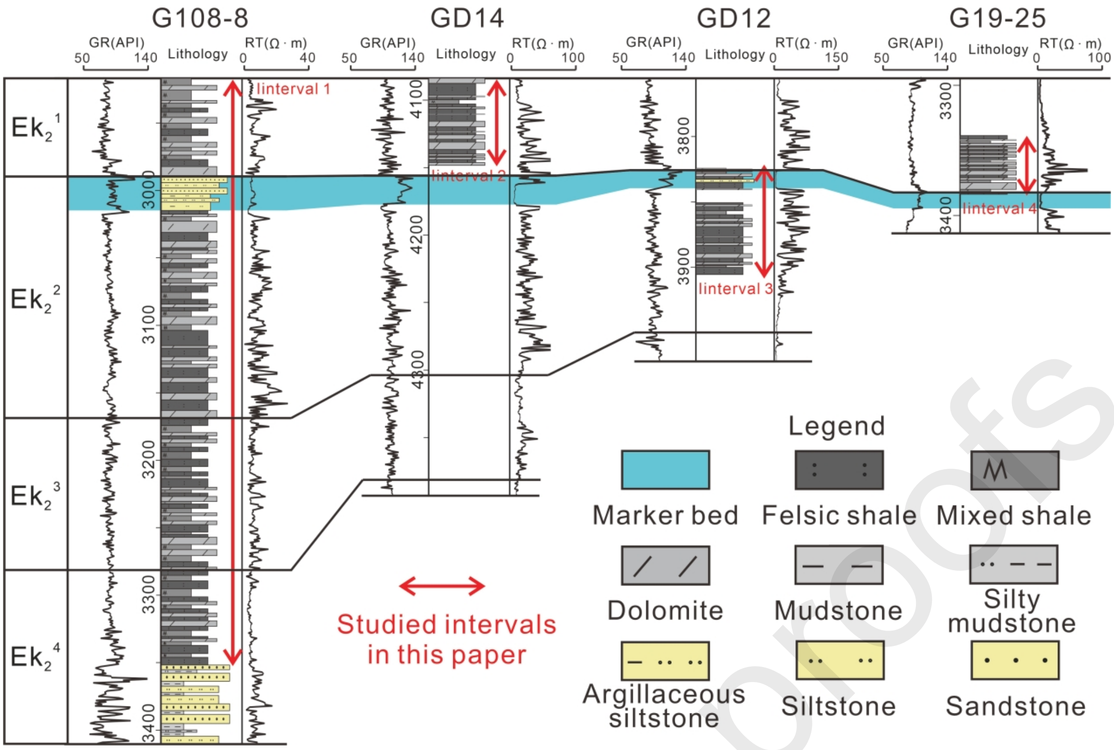

G108-8
GD14
GD12
G19-25
GR(API)
Lithology
RT(Ω · m)
Ek2 1
Ek2 2
Ek2 3
Ek2 4
linterval 1
linterval 2
linterval 3
linterval 4
Studied intervals in this paper
Legend
Marker bed
Felsic shale
Mixed shale
Dolomite
Mudstone
Silty mudstone
Argillaceous siltstone
Siltstone
Sandstone

820 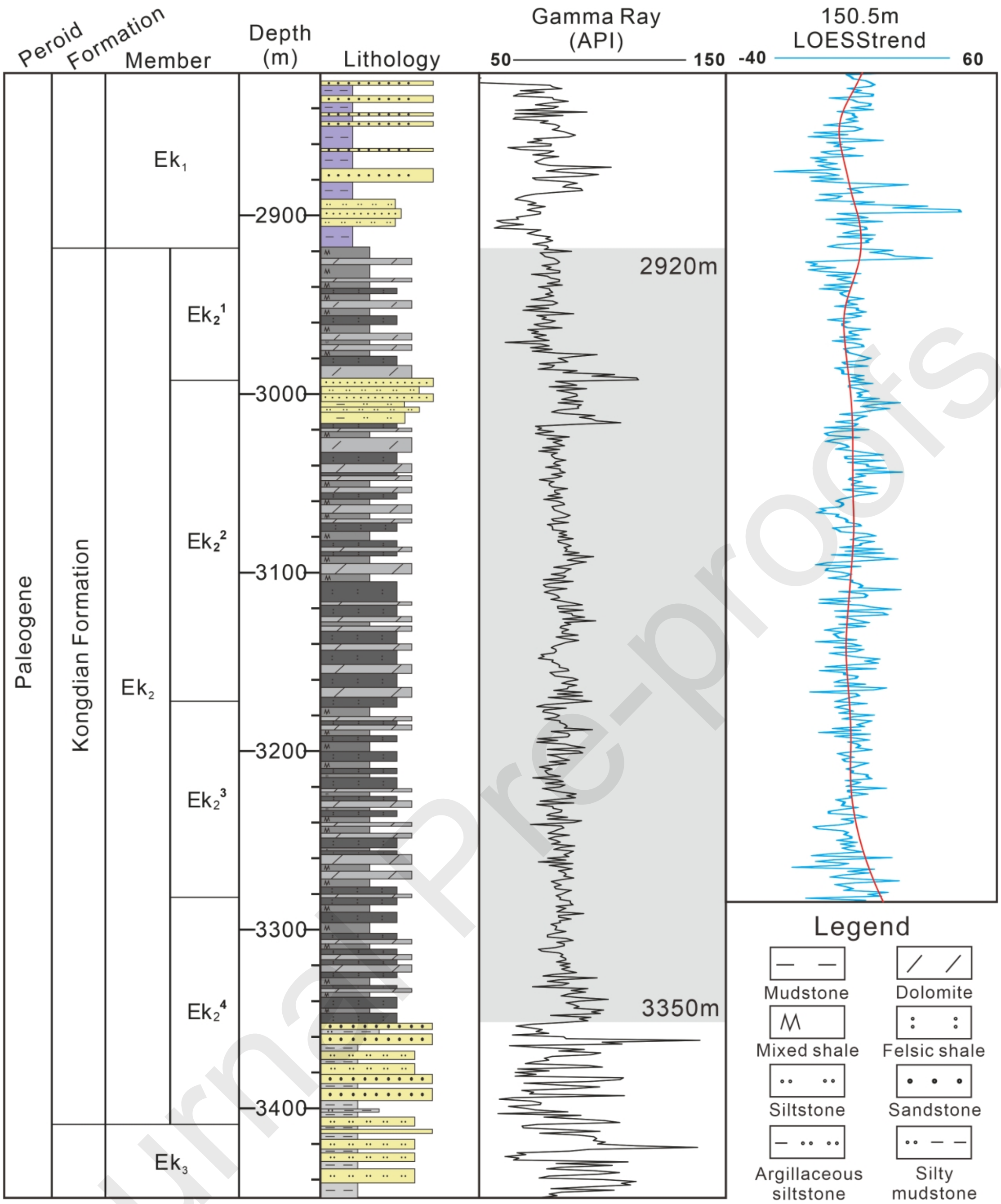

Peroid
Formation
Member
Depth (m)
Lithology
Gamma Ray (API)
50
150
150.5m LOESStrend
-40
60
Paleogene
Kongdian Formation
Ek1
Ek2
Ek3
Ek2 1
Ek2 2
Ek2 3
Ek2 4
2900
3000
3100
3200
3300
3400
2920m
3350m
Legend
Mudstone
Dolomite
Mixed shale
Felsic shale
Siltstone
Sandstone
Argillaceous siltstone
Silty mudstone

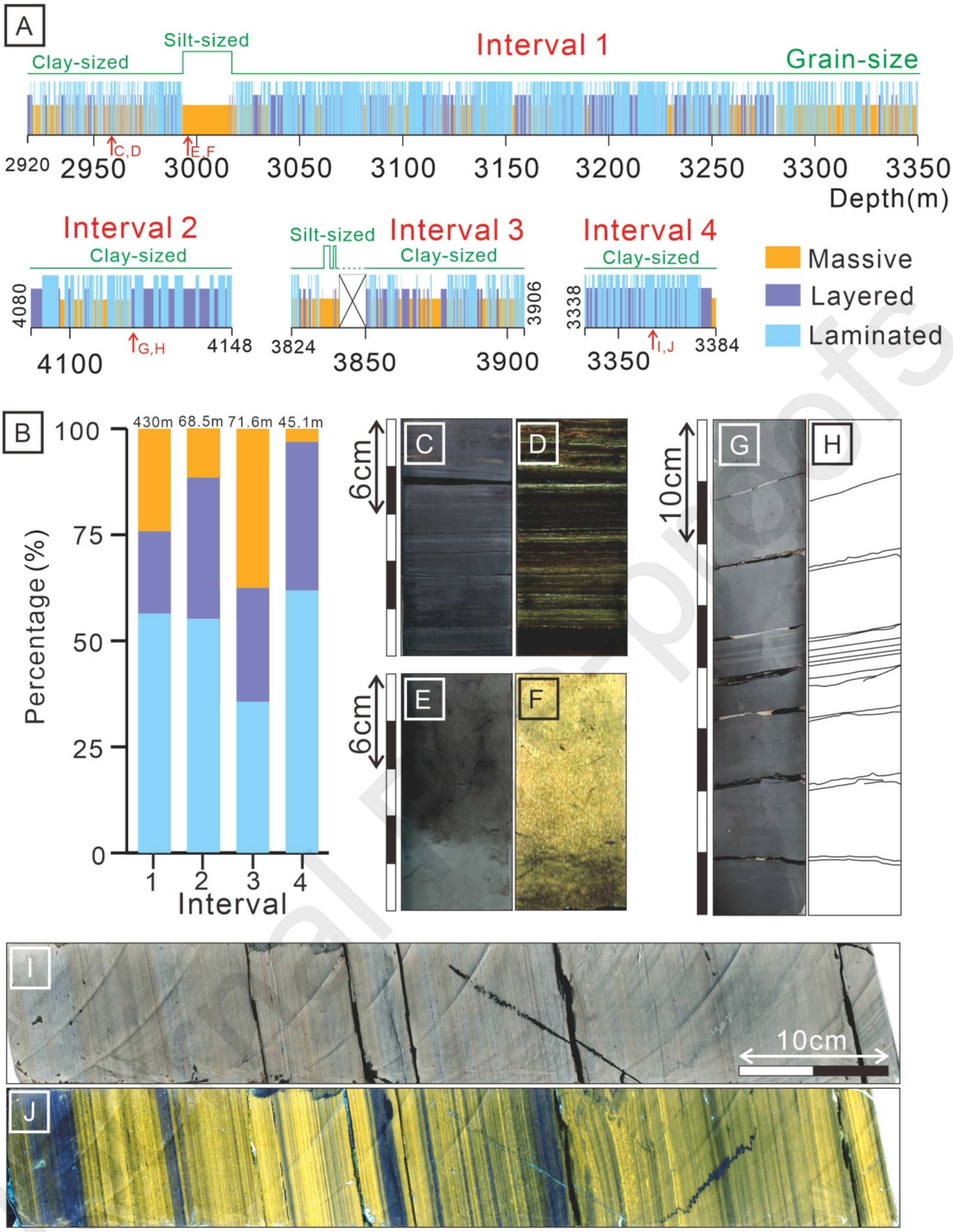
A
Clay-sized
Silt-sized
Interval 1
Grain-size
C,D
E,F
2920
2950
3000
3050
3100
3150
3200
3250
3300
3350
Depth(m)
Interval 2
Clay-sized
4080
4100
G,H
4148
Silt-sized
Interval 3
Clay-sized
3824
3850
3900
3906
Interval 4
Clay-sized
3338
3350
I,J
3384
Massive
Layered
Laminated
B
430m
68.5m
71.6m
45.1m
Percentage (%)
100
75
50
25
0
1
2
3
4
Interval
6cm
C
D
E
F
10cm
G
H
I
10cm
J

821

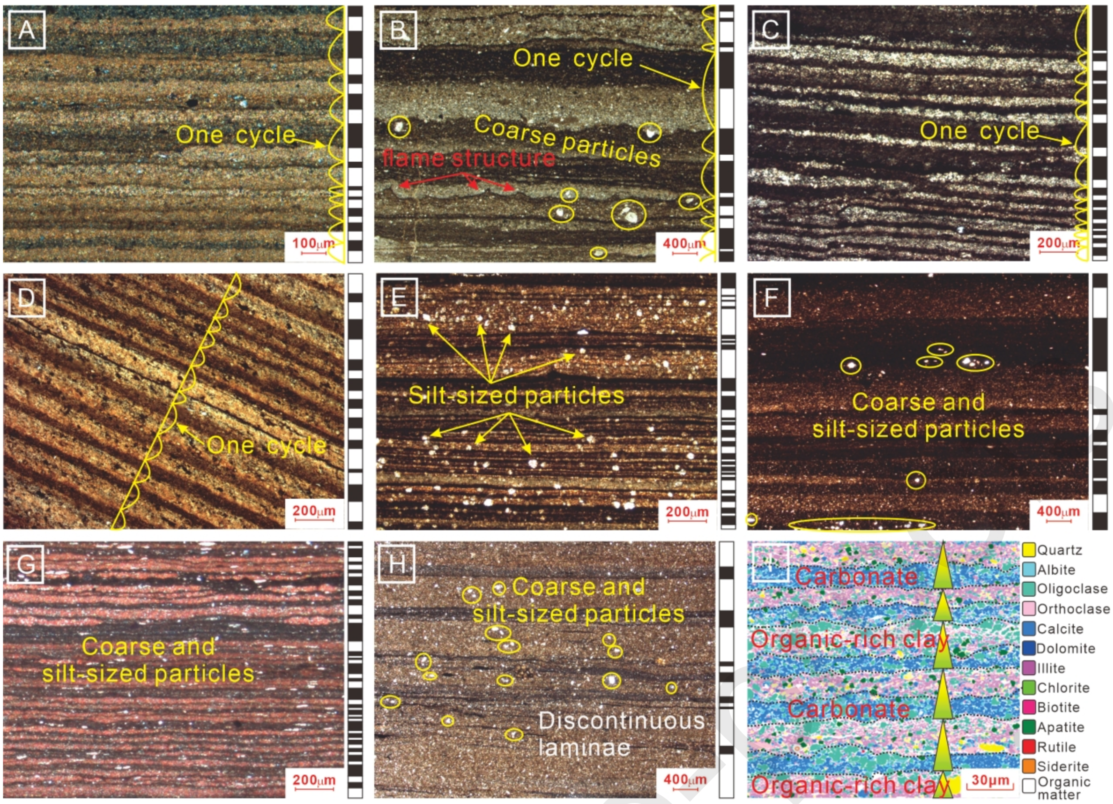
A
One cycle
100μm
B
One cycle
Coarse particles
flame structure
400μm
C
One cycle
200μm
D
One cycle
200μm
E
Silt-sized particles
200μm
F
Coarse and
silt-sized particles
400μm
G
Coarse and
silt-sized particles
200μm
H
Coarse and
silt-sized particles
Discontinuous
laminae
400μm
I
Carbonate
Organic-rich clay
Carbonate
Organic-rich clay
30μm
Quartz
Albite
Oligoclase
Orthoclase
Calcite
Dolomite
Illite
Chlorite
Biotite
Apatite
Rutile
Siderite
Organic matter

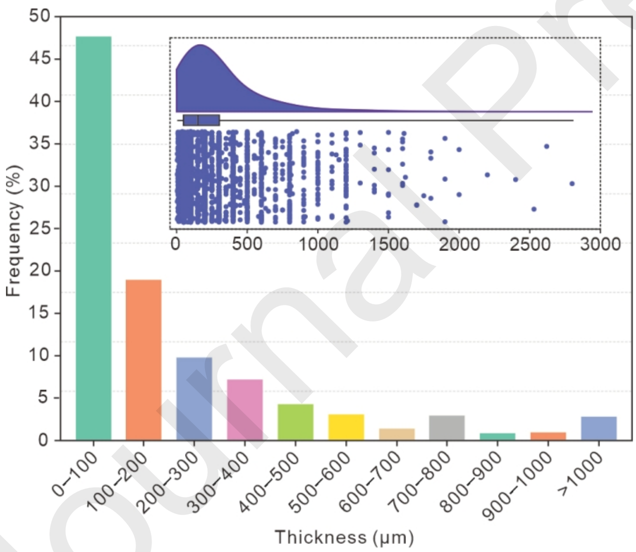
Frequency (%)
Thickness (μm)
0–100
100–200
200–300
300–400
400–500
500–600
600–700
700–800
800–900
900–1000
>1000
0
500
1000
1500
2000
2500
3000

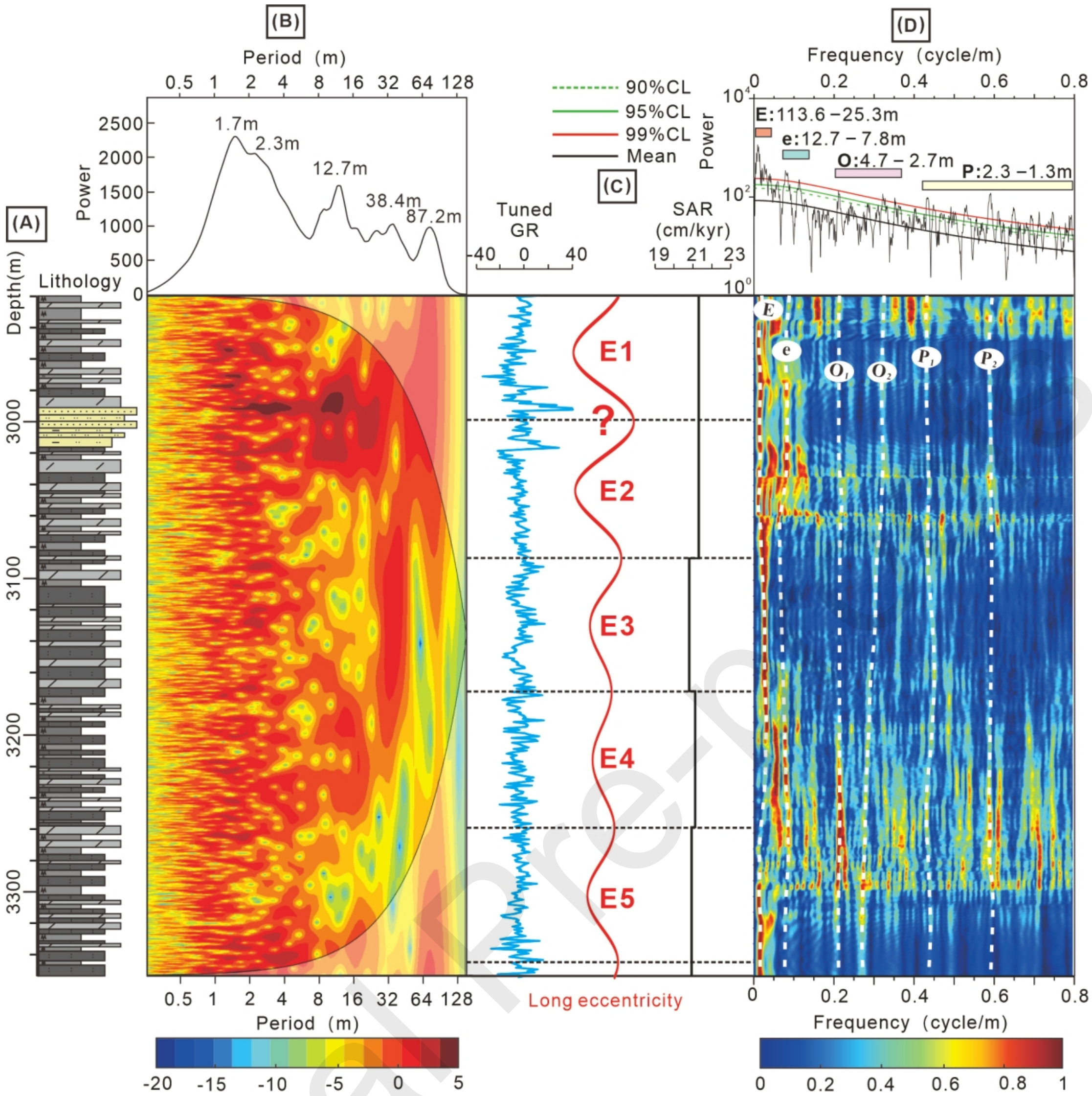
(A)
Depth(m)
Lithology
3000
3100
3200
3300
(B)
Period (m)
0.5 1 2 4 8 16 32 64 128
Power
2500
2000
1500
1000
500
0
1.7m
2.3m
12.7m
38.4m
87.2m
-20 -15 -10 -5 0 5
(C)
90%CL
95%CL
99%CL
Mean
Tuned GR
-40 0 40
SAR (cm/kyr)
19 21 23
E1
E2
E3
E4
E5
?
Long eccentricity
(D)
Frequency (cycle/m)
0 0.2 0.4 0.6 0.8
E:113.6 – 25.3m
e:12.7 – 7.8m
O:4.7 – 2.7m
P:2.3 – 1.3m
0 0.2 0.4 0.6 0.8 1

824

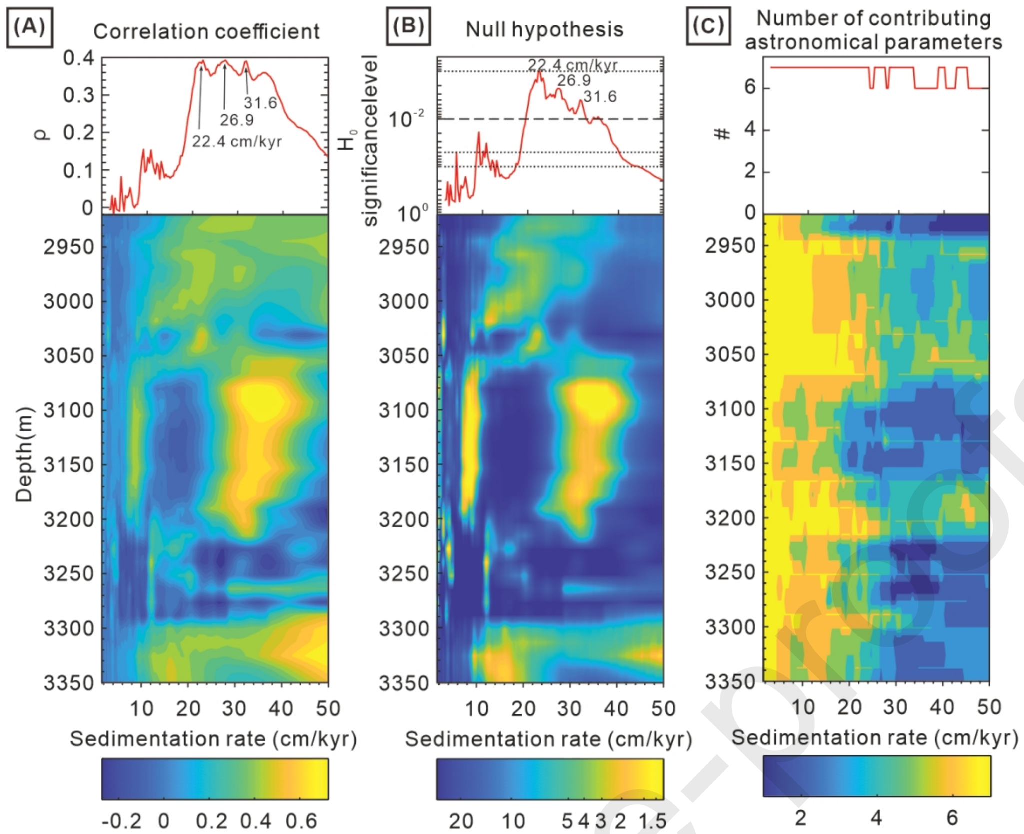
(A)
Correlation coefficient
ρ
22.4 cm/kyr
26.9
31.6
Depth(m)
Sedimentation rate (cm/kyr)
(B)
Null hypothesis
H0 significancelevel
22.4 cm/kyr
26.9
31.6
Sedimentation rate (cm/kyr)
(C)
Number of contributing astronomical parameters
#
Sedimentation rate (cm/kyr)

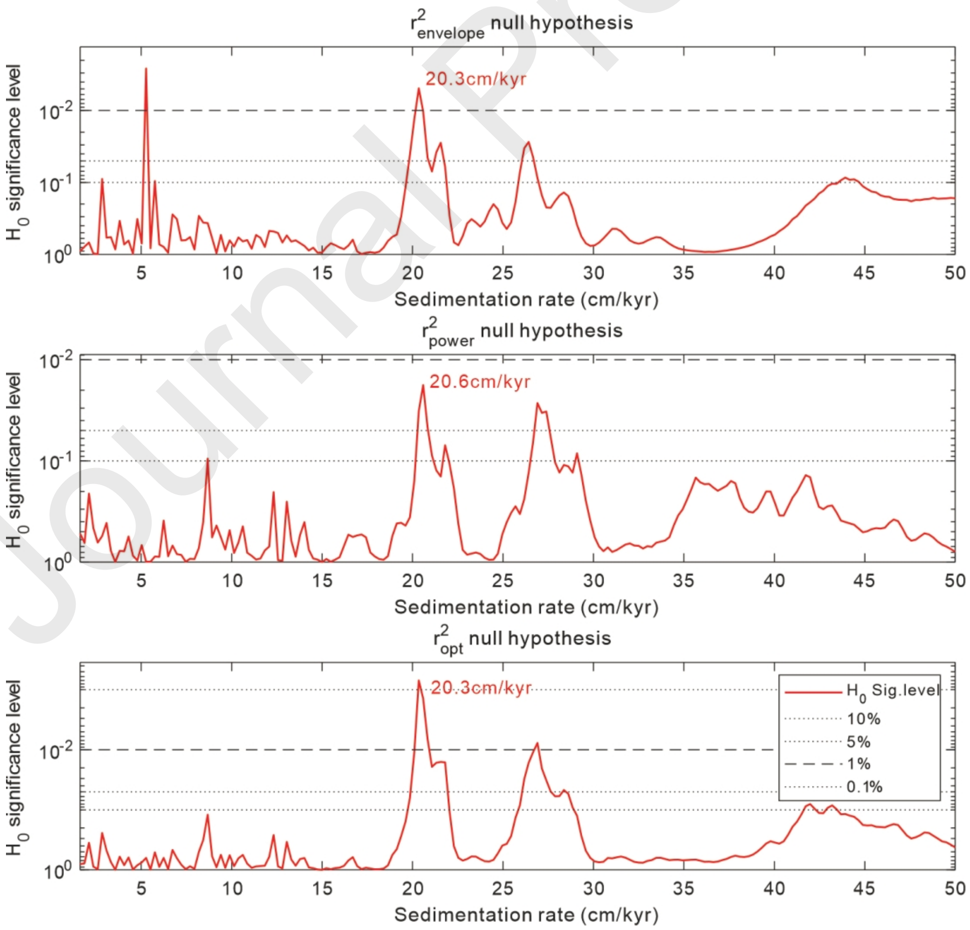
r2envelope null hypothesis
H0 significance level
20.3cm/kyr
Sedimentation rate (cm/kyr)
r2power null hypothesis
H0 significance level
20.6cm/kyr
Sedimentation rate (cm/kyr)
r2opt null hypothesis
H0 significance level
20.3cm/kyr
H0 Sig.level
10%
5%
1%
0.1%
Sedimentation rate (cm/kyr)

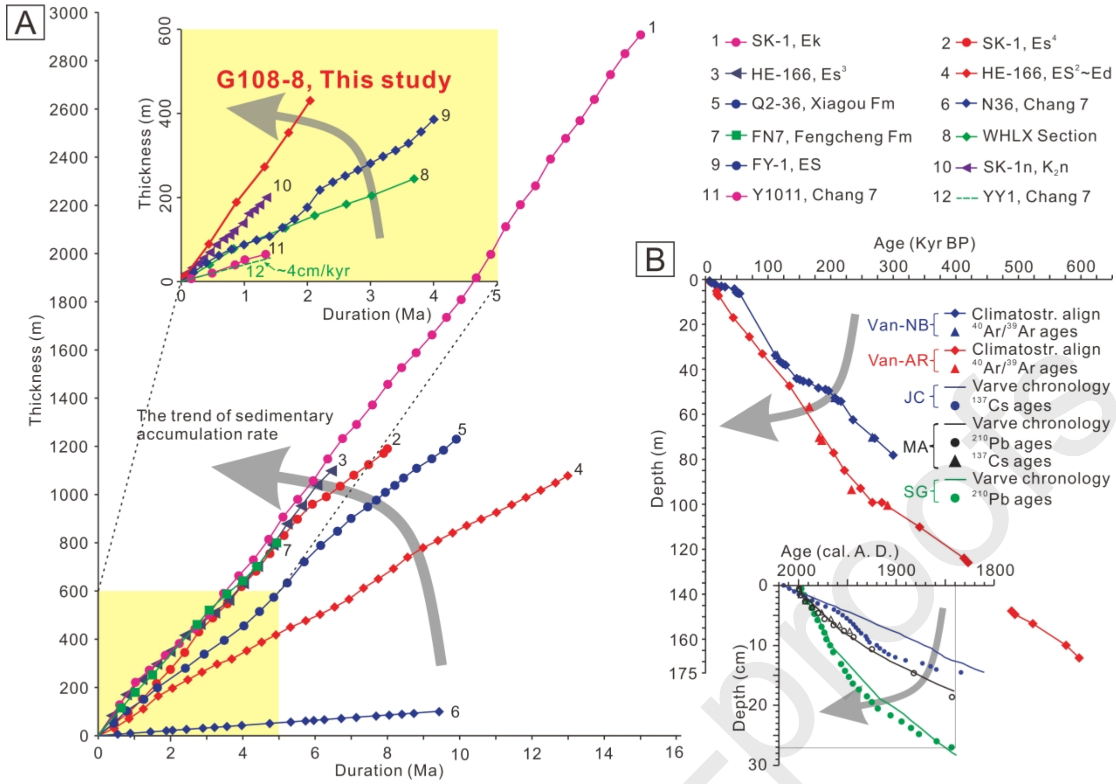
A
Thickness (m)
Duration (Ma)
G108-8, This study
~4cm/kyr
The trend of sedimentary accumulation rate
1 SK-1, Ek
2 SK-1, Es⁴
3 HE-166, Es³
4 HE-166, ES²~Ed
5 Q2-36, Xiagou Fm
6 N36, Chang 7
7 FN7, Fengcheng Fm
8 WHLX Section
9 FY-1, ES
10 SK-1n, K₂n
11 Y1011, Chang 7
12 YY1, Chang 7
B
Age (Kyr BP)
Depth (m)
Van-NB
Climatostr. align
⁴⁰Ar/³⁹Ar ages
Van-AR
Climatostr. align
⁴⁰Ar/³⁹Ar ages
JC
Varve chronology
¹³⁷Cs ages
MA
Varve chronology
²¹⁰Pb ages
¹³⁷Cs ages
SG
Varve chronology
²¹⁰Pb ages
Age (cal. A. D.)
Depth (cm)

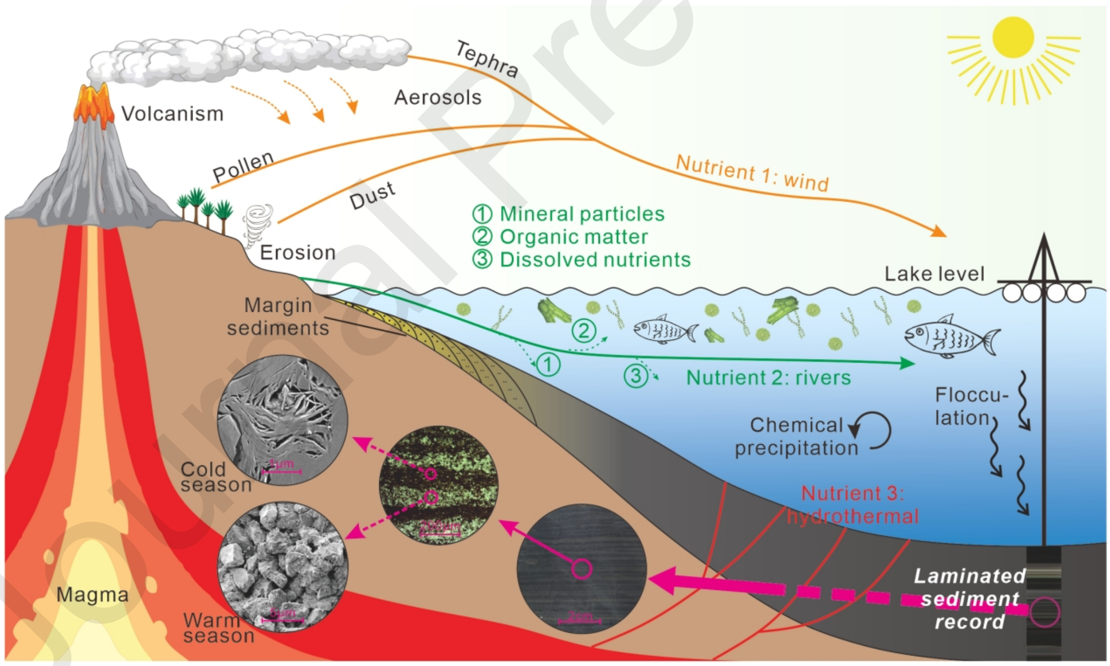
Tephra
Aerosols
Volcanism
Pollen
Dust
Nutrient 1: wind
Erosion
① Mineral particles
② Organic matter
③ Dissolved nutrients
Lake level
Margin sediments
Nutrient 2: rivers
Flocculation
Chemical precipitation
Cold season
Nutrient 3: hydrothermal
Magma
Warm season
Laminated sediment record

829

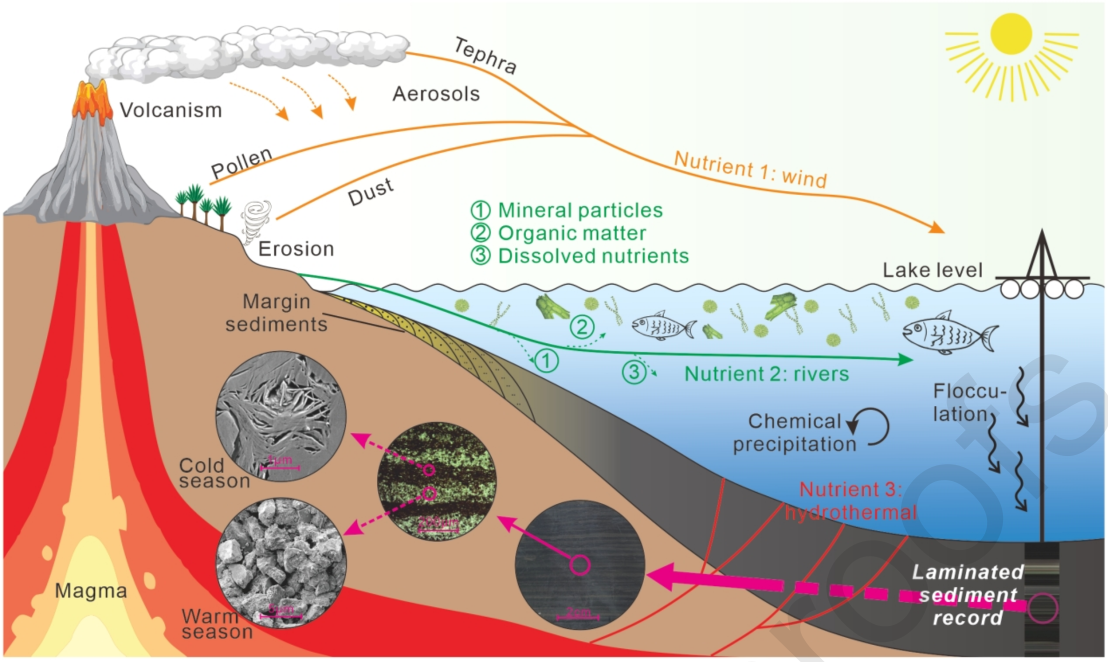

Tephra
Aerosols
Volcanism
Pollen
Dust
Nutrient 1: wind
Erosion
① Mineral particles
② Organic matter
③ Dissolved nutrients
Lake level
Margin
sediments
Nutrient 2: rivers
Flocculation
Chemical
precipitation
Cold
season
Nutrient 3:
hydrothermal
Magma
Warm
season
Laminated
sediment
record